Journal of Computational and Applied Mathematics 376 (2020) 112862

Contents lists available at ScienceDirect

Journal of Computational and Applied Mathematics

journal homepage: www.elsevier.com/locate/cam

A hybrid method and unified analysis of generalized finite differences and Lagrange finite elements

Rebecca Conley [a], Tristan J. Delaney [b,1], Xiangmin Jiao [b,*]

[a] Department of Mathematics, Saint Peter's University, Jersey City, NJ 07306, USA
[b] Department of Applied Mathematics & Statistics and Institute for Advanced Computational Science, Stony Brook University, Stony Brook, NY 11794, USA

ARTICLE INFO

Article history:
Received 16 June 2019
Received in revised form 17 January 2020

MSC:
65N06
65N30
65N12

Keywords:
Partial differential equations
Finite element methods
Generalized finite differences
Generalized weighted residuals
Stability
Convergence

ABSTRACT

Finite differences, finite elements, and their generalizations are widely used for solving partial differential equations, and their high-order variants have respective advantages and disadvantages. Traditionally, these methods are treated as different (strong vs. weak) formulations and are analyzed using different techniques (Fourier analysis or Green's functions vs. functional analysis), except for some special cases on regular grids. Recently, the authors introduced a hybrid method, called *Adaptive Extended Stencil FEM* or *AES-FEM* (Conley et al., 2016), which combines features of *generalized finite differences* and *Lagrange finite elements* to achieve second-order accuracy over unstructured meshes. However, its analysis was incomplete due to the lack of existing mathematical theory that unifies the formulations and analysis of these different methods. In this work, we introduce the framework of *generalized weighted residuals* to unify the formulation of finite differences, finite elements, and AES-FEM. In addition, we propose a unified analysis of the *well-posedness*, *convergence*, and *mesh-quality dependency* of these different methods. We also report numerical results with AES-FEM to verify our analysis. We show that AES-FEM improves the accuracy of generalized finite differences while reducing the mesh-quality dependency and simplifying the implementation of high-order finite elements.

1. Introduction

Finite differences, finite elements, and their generalizations are widely used for solving partial differential equations (PDEs), or more precisely, for the spatial discretization for their associated boundary value problems (BVPs). The finite difference methods (FDM) are standard techniques in numerical analysis [1,2] and are widely used for solving hyperbolic PDEs in computational fluid dynamics. The finite element methods (FEM), on the other hand, are the most successful method for solving elliptic and parabolic PDEs (e.g., [3,4]). Since many PDEs, such as advection–diffusion–reaction equations, Navier–Stokes equations, etc., are multiphysics in nature, involving both parabolic (elliptic) and hyperbolic components, it has been of great interest for applied mathematicians to develop hybrid methods that combine the advantages of FEM and FDM. The most notable examples are *discontinuous Galerkin* methods [5,6] and some *finite volume methods* [7,8], which use discontinuous test functions analogous to the *nonconforming finite elements* [9, Section 10.3] and

* Corresponding author.
E-mail addresses: rconley@saintpeters.edu (R. Conley), tristan.delaney@synopsys.com (T.J. Delaney), xiangmin.jiao@stonybrook.edu (X. Jiao).
[1] Current address: Synopsys, Inc., Mountain View, CA 94043, USA.

https://doi.org/10.1016/j.cam.2020.112862
0377-0427/

use finite-difference style computations of interface fluxes or jump conditions (such as WENO [10,11] and Lax–Friedrichs limiters [7, p. 199]) along element or cell boundaries.

In [12,13], the authors introduced a new hybrid method, called the *adaptive extended stencil finite element method* or *AES-FEM*. Like Lagrange finite elements, AES-FEM has C^0 continuous test functions, so there are no explicit interface and jump conditions in its variational forms, unlike nonconforming finite elements. However, unlike finite elements, AES-FEM uses least-squares based trial functions similar to those of generalized finite differences [14]. We refer to these trial functions as *generalized Lagrange polynomial* (GLP) basis functions, which are not C^0 *continuous* but have similar properties to Lagrange interpolation. The GLP basis functions introduce a "variational crime" (cf. Appendix D.3), which is similar to, but yet different from, that of other nonconforming finite elements. The analysis of GLP-based methods, including generalized finite difference method (GFDM) and AES-FEM, requires a mathematical analysis that unifies the classical analysis of finite differences and finite elements. This unification is the primary goal of this work, which will reveal some insights from a theoretical point of view, and also enable a rigorous generalization of AES-FEM to higher-order accuracy from a practical point of view.

The main contributions of this work are as follows. First, we unify the formulations of GFDM, FEM, and AES-FEM under the framework of *generalized weighted residuals* (GWR), of which the trial functions are either Lagrange or generalized Lagrange basis functions. Second, we establish the conditions for *well-posedness*, *convergence*, and *superconvergence* of GFDM and AES-FEM, and compare their mesh-quality requirements against Lagrange finite elements. Third, we prove and also demonstrate the high-order convergence of AES-FEM. For simplicity, we assume exact geometry for Neumann boundaries in this paper, and we defer the treatment of Neumann boundary conditions over approximate curved boundaries to future work.

The remainder of the paper is organized as follows. Section 2 reviews the (G)FDM and FEM for boundary value problems, as well as their respective classical analyses. Section 3 introduces the concept of *generalized Lagrange polynomial* basis functions and the framework of *generalized weighted residuals* (GWR), which unifies the formulations of GFDM, FEM, and AES-FEM. Section 4 analyzes the well-posedness of GWR methods. Section 5 addresses the convergence of GFDM and AES-FEM to confirm our analysis. Section 6 presents some numerical results. Section 7 concludes this paper with a discussion on future work.

2. Background and preliminaries

In this section, we briefly review finite differences, finite elements, and some of their generalizations for boundary value problems. We refer readers to [15] for a brief history of these different methods. For completeness, we review some relevant details about the generalized Lagrange polynomials, AES-FEM, and functional analysis in the appendices.

2.1. Boundary value problems

Let $\Omega \subset \mathbb{R}^d$ be a bounded, piecewise smooth domain with boundary $\Gamma = \Gamma_D \cup \Gamma_N$, where d is typically 2 or 3, and Γ_D and Γ_N denote the Dirichlet and Neumann boundaries, respectively. Let $\mathcal{L}$ be a second-order linear differential operator. In general, $\mathcal{L}$ has the form of

$$\mathcal{L}u = -\nabla \cdot (\mu \nabla u) + \boldsymbol{v} \cdot \nabla u + \omega^2 u, \tag{2.1}$$

where ∇ and $\nabla\cdot$ denote the gradient and divergence operators, $\mu(\boldsymbol{x}) : \Omega \to \mathbb{R}^+$ corresponds to a diffusion coefficient, $\boldsymbol{v} : \Omega \to \mathbb{R}^d$ is a velocity field, and $\omega : \Omega \to \mathbb{R}$ is a wavenumber or frequency. Typically, $\nabla \cdot \boldsymbol{v} = 0$. A second-order partial differential equation has the form of

$$\mathcal{L}u = f \quad \text{on } \Omega, \tag{2.2}$$

where $f : \Omega \to \mathbb{R}$ is a source term. This general form is known as the *advection–diffusion–reaction* equations for vector-valued PDEs. For simplicity, we focus on scalar fields and assume *diffusion dominance* (i.e., $\mu(\boldsymbol{x}) \geq C \|\boldsymbol{v}(\boldsymbol{x})\| h$ for some $C \geq 1$, where h denotes some characteristic edge length of the mesh; cf. Appendix D). If $\omega = 0$, then its corresponding PDE is the *advection–diffusion equation*. A *boundary value problem* (BVP) corresponding to the above PDE may have some *Dirichlet boundary conditions*

$$u = u_D \quad \text{on } \Gamma_D, \tag{2.3}$$

and potentially some *Neumann boundary conditions*

$$\mu \partial_{\boldsymbol{n}} u = g_N \quad \text{on } \Gamma_N, \tag{2.4}$$

where $\partial_{\boldsymbol{n}}$ denotes the normal derivative, i.e., $\partial_{\boldsymbol{n}} \equiv \boldsymbol{n} \cdot \nabla$. The boundary condition is said to be *homogeneous* if $\Gamma_D = \Gamma$ and $u_D = 0$.

2.2. Finite differences and their generalizations

The finite difference methods (FDM) are arguably the simplest and the best known numerical methods for solving initial and boundary value problems; see textbooks such as [1,2]. In a nutshell, FDM approximates the partial derivatives in (2.1) using finite difference operators, which result in a system of algebraic equations $\boldsymbol{A}\boldsymbol{x} = \boldsymbol{b}$. The analysis of FDM is also conceptually simple: If the truncation errors in each algebraic equation are *consistent* (i.e., $\mathcal{O}(h^k)$ for some $k > 0$ as the edge length h tends to 0) and the *absolute condition number* of the algebraic system (i.e., $\left\|\boldsymbol{A}^{-1}\right\|$) is bounded independently of h (i.e., $\mathcal{O}(1)$), then the finite difference method converges in exact arithmetic. This condition is known as the *fundamental theorem of numerical analysis* and is simply stated as "*consistency and stability imply convergence*" [3, p. 124]. The main argument then involves bounding the absolute condition number, which traditionally is done using Fourier analysis on regular grids [1, p. 20] or using Green's functions in 1D [1, p. 22]. The effect of rounding errors is typically omitted in the analysis of BVPs, but it has been considered by some authors; see e.g. [16–18].

The classical FDM is limited to structured meshes because the finite difference operators are defined based on 1D polynomial interpolations locally at each node in a dimension-by-dimension fashion. The same approach can be utilized on curvilinear meshes for curved but relatively simple geometries; see e.g. [19]. Some authors have considered its generalizations to unstructured meshes or point clouds; see e.g. [14,20–22]. Finite difference operators have been generalized to use least-squares approximations; see e.g. [14,20,21]. In this work, we use *generalized finite differences* (*GFD*) to refer to the least-squares-based finite difference operators and use *generalized finite difference methods* (*GFDM*) to refer to the methods that use these GFD operators to convert (2.2) directly into algebraic equations. To the best of our knowledge, there was no prior complete convergence analysis of GFDM for BVPs, except for local consistency using Taylor series and the temporal aspect of stability for time-dependent PDEs [14,23–25].

2.3. Finite elements and weighted residuals

The finite element methods (FEM) are among the most powerful and successful methods for solving BVPs. Mathematically, FEM can be expressed using the framework of *weighted residuals* [26], also known as *variational formulations* [9, p. 2]. Let Ω_h denote the approximation of the domain Ω with a mesh. Without loss of generality, let us assume triangular or tetrahedral meshes, and let n denote the number of nodes in $\Omega_h \backslash \Gamma_D$. Let u_h denote the approximate solution of the PDE on Ω. The *residual* of (2.2) corresponding to u_h is $\mathcal{L}u_h - f$. Let $\{\psi_i \mid 1 \leq i \leq n\}$ denote the set of *test* (*or weight*) *functions*, which span the *test space* Ψ. A *weighted residual method* requires the residual to be orthogonal to Ψ over Ω, or equivalently,

$$\int_\Omega \mathcal{L}u_h \psi_i \, d\boldsymbol{x} = \int_\Omega f \psi_i \, d\boldsymbol{x}, \quad \text{for } i = 1, \ldots, n. \tag{2.5}$$

In FEM, the test functions ψ_i are (weakly) differentiable and have local support.

To discretize the problem fully, let $\{\phi_j \mid 1 \leq j \leq n\}$ denote a set of basis functions, which span the *trial space* Φ. Let $\boldsymbol{\Phi}$ denote the vector containing ϕ_j. We find the approximate solution u_h in Φ, i.e.,

$$u \approx u_h = \boldsymbol{\Phi}^T \boldsymbol{u}_h, \tag{2.6}$$

where $\boldsymbol{u}_h$ is the unknown vector. The basis functions are *Lagrange* if $\phi_j(\boldsymbol{x}_i) = \delta_{ij}$, the Kronecker delta function; i.e., $\phi_j(\boldsymbol{x}_i) = 1$ if $i = j$ and $\phi_j(\boldsymbol{x}_i) = 0$ if $i \neq j$. With Lagrange basis functions, let $\boldsymbol{u}_I$ denote the vector composed of $u(\boldsymbol{x}_j)$. Then, $u_I = \boldsymbol{\Phi}^T \boldsymbol{u}_I$ is the *interpolation* of u in Φ. Furthermore, the unknown vector $\boldsymbol{u}_h$ in (2.6) is composed of approximations to nodal values $u(\boldsymbol{x}_j)$. The FEM using Lagrange basis functions is called *Lagrange FEM* [27, p. 36]. In this work, FEM refers to Lagrange FEM, unless otherwise noted.

For elliptic PDEs, FEM solves (2.5) by performing integration by parts and then substituting the boundary conditions (2.3) and (2.4) into the resulting integral equation. Let $\langle \cdot, \cdot \rangle_\Omega$ denote the inner product over Ω,[2] i.e.,

$$\langle \phi, \psi \rangle_\Omega = \int_\Omega \phi \psi \, d\boldsymbol{x}, \tag{2.7}$$

which defines the L^2 norm over Ω, i.e., $\|\phi\|_{L^2(\Omega)} = \sqrt{\langle \phi, \phi \rangle_\Omega}$. Similarly, let $\langle \cdot, \cdot \rangle_\Gamma$ denote the inner product over Γ. For the general linear operator $\mathcal{L}$ in (2.1), after integration by parts of the first term, we obtain a variational form for each test function ψ_i

$$a(u_h, \psi_i) = \langle f, \psi_i \rangle_\Omega + \langle \mu \partial_{\boldsymbol{n}} u_h, \psi_i \rangle_\Gamma \,, \tag{2.8}$$

where

$$a(u_h, \psi_i) = \int_\Omega \left(\nabla \psi_i \cdot (\mu \nabla u_h) + \boldsymbol{v} \cdot \nabla u_h \psi_i + \omega^2 u_h \psi_i \right) d\boldsymbol{x}, \tag{2.9}$$

is the *bilinear form*.

[2] In functional analysis, the inner product is denoted as $(\cdot, \cdot)$. We use $\langle \cdot, \cdot \rangle_\Omega$ for clarity and for distinguishing the inner products on Ω and on boundary Γ. See Appendix D for a review of some relevant functional analysis concepts.

2.4. Prior efforts on unified analysis of FDM and FEM

The unification of the accuracy and stability analysis of FDM and FEM has been of great interest to numerical analysts since the late 1960s [28,3]. In terms of local error analysis, this unification is straightforward by using Taylor series, except that FDM traditionally relied on 1D Taylor series, whereas FEM requires the higher-dimensional version. In terms of global error analysis, Fix and Strang explored adapting Fourier analysis from FDM to FEM on structured grids [28]. Another common technique used in analyzing both FDM and FEM is the Green's functions. It was particularly successful for proving the convergence of FDM and superconvergence of FEM in ℓ^∞ norm in 1D or with tensor-product elements; see, e.g., [29,30,1]. In this work, we unify the analysis of well-posedness of GFDM, FEM, and AES-FEM by integrating functional analysis and approximation theory.

3. Generalized weighted residuals

To unify the formulations and analysis of GFDM, FEM, and AES-FEM, we need a mathematical framework that is more general than weighted residuals. The framework, which we refer to as *generalized weighted residuals* (*GWR*), has three components: a mesh and its associated test functions and geometric realization, a set of (generalized) Lagrange basis functions, and a (generalized) variational form. We address these three components using GFDM and FEM as examples, and then introduce AES-FEM under this framework.

3.1. Component 1: Meshes, test functions, and geometry

3.1.1. Meshes

Like in FEM, in GWR the domain Ω is tessellated by a *mesh*, which is typically simplicial or rectangular. Without loss of generality, we assume simplicial meshes in this work, which are triangular in 2D or tetrahedral in 3D. The triangles and tetrahedra are known as the *elements*, of which the vertices are called the *nodes*. Let Ω_h denote the union of the geometric realizations of the elements, and let $\partial\Omega_h$ denote its boundary. Let Γ_h denote an approximation of Γ. We assume Γ_h is the same as $\partial\Omega_h$. Let $\Omega_h = \Omega_h^\circ \cup \Gamma_{h,N}^\circ \cup \Gamma_{h,D}$, where Ω_h° denotes the interior of Ω_h, $\Gamma_{h,D}$ denotes the approximation to the Dirichlet boundary, and $\Gamma_{h,N}^\circ = \Gamma_h \backslash \Gamma_{h,D}$. We refer to the nodes in Ω_h°, $\Gamma_{h,N}^\circ$, and $\Gamma_{h,D}$ as *interior*, *Neumann*, and *Dirichlet* nodes, respectively. Without loss of generality, we assume the nodes are numbered between 1 and m, where the first n nodes are those in $\Omega_h^\circ \cup \Gamma_{h,N}^\circ$.

Given a node $\boldsymbol{x}$, the term *stencil* refers to the nodes where the generalized Lagrange trial functions associated with $\boldsymbol{x}$ are non-zero. Note that in GFDM, stencils are referred to as *stars* [31–33]. See Appendix B for details about stencil selection for AES-FEM.

3.1.2. Test functions

In GWR, there is a *test function* ψ_i associated with each node $\boldsymbol{x}_i \in \Omega_h$, analogous to those in (2.5). Each test function ψ_i has *local support*, denoted by Ω_i, which is the closure of the subset of points in Ω_h such that $\psi_i(\boldsymbol{x}) \neq 0$, i.e., $\Omega_i = \mathrm{cl}(\{\boldsymbol{x} \mid \boldsymbol{x} \in \Omega_h \wedge \psi_i(\boldsymbol{x}) \neq 0\})$. Topologically, the local support is *compact*, in that it contains only a small constant number of nodes. In a Lagrange FEM, each test function is a Lagrange basis function, such as a hat (a.k.a. pyramid) function. Note that the test functions in FEM may be quadratic or higher-degree polynomials, which have *mid-edge*, *mid-face*, and *mid-cell* nodes, besides the *corner* nodes. For FEM, the local support Ω_i is composed of the union of the elements incident on $\boldsymbol{x}_i$. For GFDM over an unstructured mesh, within the GWR framework, the test function at $\boldsymbol{x}_i$ is the Dirac delta function at $\boldsymbol{x}_i$, and the local support of a Dirac delta function is $\boldsymbol{x}_i$ itself. We will discuss this further in Section 3.3.

Remark 1. In [27], Ciarlet defined a finite element method as a triplet: a mesh, element-based (nearly) polynomial basis, and node-based basis functions of an H^1 space. A GWR is more general in that the test functions may not span an L^2 or H^1 space, which is the case in (generalized) finite difference methods.

3.1.3. Geometric realizations

For numerical computations, the local support Ω_i must have a *geometric realization*, which is the union of the geometric realizations of its elements. For each element τ, its geometric realization is defined through a mapping from a *master element* e_m in the parametric space to the "physical space" $\mathbb{R}^d$. Let $\boldsymbol{\xi}$ denote the natural coordinates in the parametric space. Let n_e denote the number of nodes in e_m, and let $\boldsymbol{\xi}_K$ and $\boldsymbol{x}_K$ denote the natural coordinates and physical coordinates, respectively, of the Kth node in e_m, where $1 \leq K \leq n_e$. For example, a linear triangle has nodes $\boldsymbol{\xi}_1 = [0, 0]$, $\boldsymbol{\xi}_2 = [0, 1]$ and $\boldsymbol{\xi}_3 = [1, 0]$. The *geometric realization* of an element τ is defined by a Lagrange interpolation

$$\boldsymbol{x}_\tau(\boldsymbol{\xi}) = \sum_{K=1}^{N_e} \boldsymbol{x}_K \varphi_K(\boldsymbol{\xi}), \tag{3.1}$$

where K is the local nodal ID in τ for the kth node in Ω_h. The functions φ_K are in general polynomials. Using the interpolation theory [34], given n_e nodes and an equal number of monomials in $\boldsymbol{\xi}$, if the Vandermonde system in the

parametric space is stable, then the basis functions $\{\varphi_k\}$ are uniquely determined over e_m. In FEM, the geometric basis functions $\{\varphi_k\}$ do not need to be the same as the test functions $\{\psi_i\}$ (and trial functions $\{\phi_j\}$).

Besides the local support, we also define a "*control volume*" ω_i for each node to facilitate the theoretical analysis in Section 4 by generalizing its traditional definition. Let $|\omega_i|$ denote the Lebesgue measure (namely, the area or volume) of ω_i. The control volumes of all the nodes partition Ω_h, i.e., $\Omega_h = \cup_{i=1}^m \omega_i$ and $|\omega_i \cap \omega_j| = 0$ if $i \neq j$. For FEM, the control volume of a node can be defined by the union of its closest points within its incident elements. For GFDM, we define the control volume similarly or use the Voronoi cells. Note that these control volumes are not used in computations; instead, we will use them in analyzing well-posedness and convergence. See Fig. B.6 in Appendix B for an example of a control volume.

3.1.4. Approximation power of Lagrange finite elements

In FEM, the test (and trial) functions are Lagrange functions, which are defined using a mapping from a parametric space $[0, 1]^d$ to the physical space $\mathbb{R}^d$, similar to that of the geometric basis functions. More precisely, let $\{\psi_{e,J} \mid 1 \leq J \leq n_e\}$ denote the *Lagrange polynomial basis* over the master element, which satisfies the Kronecker delta property $\psi_{e,J}(\boldsymbol{\xi}_I) = \delta_{IJ}$. Let $\boldsymbol{x}_\tau(\boldsymbol{\xi}) : [0, 1]^d \supseteq e_m \to \tau \subset \mathbb{R}^d$ denote the mapping from the parametric space to the physical space and $\boldsymbol{\xi}_\tau(\boldsymbol{x}) : \tau \to e_m$ denote its inverse mapping. A global test function $\psi_j(\boldsymbol{x}) : \Omega \to \mathbb{R}$ is then defined as

$$\psi_j(\boldsymbol{x}) = \psi_{e,J}\left(\boldsymbol{\xi}_\tau(\boldsymbol{x})\right) \quad \text{if } \boldsymbol{x} \in \tau, \tag{3.2}$$

where J is the local ID of node $\boldsymbol{x}_j$ in τ. By construction, ψ_j is a Lagrange test function over Ω. A (piecewise) smooth function $u : \Omega \to \mathbb{R}$ can be interpolated by the basis functions over Ω by

$$u_\psi(\boldsymbol{x}) := \sum_{j=1}^{m} u(\boldsymbol{x}_j)\psi_j(\boldsymbol{x}) = \sum_{J=1}^{n_e} u(\boldsymbol{x}_J)\psi_{e,J}\left(\boldsymbol{\xi}_\tau(\boldsymbol{x})\right), \quad \text{if } \boldsymbol{x} \in \tau. \tag{3.3}$$

If φ_k is piecewise linear, then the Lagrange test functions $\psi_j(\boldsymbol{x})$ are polynomials. However, if φ_k is nonlinear, then $\psi_j(\boldsymbol{x})$ are no longer polynomials. Nevertheless, $\left\|\nabla^k u_\psi - \nabla^k_{\boldsymbol{x}} u\right\|_\infty$ is approximated to $\mathcal{O}(h^{p-k+1})$ within each element if both $\left\|\nabla^i_{\boldsymbol{\xi}} \phi_{e,J}(\boldsymbol{\xi})\right\|_{L^\infty(e_m)}$ and $\left\|h^i \nabla^i_{\boldsymbol{x}} \boldsymbol{\xi}\right\|_{L^\infty(e_m)}$ are bounded for $i = 1, \ldots, p+1$ [35], where ∇^k denotes the kth derivative tensor and h is an edge length measure.

3.2. Component 2: Generalized Lagrange trial functions

In GWR, for each node (and more generally, at each point) in Ω_h, there is a set of *generalized Lagrange* trial functions, which may or may not be polynomials, and which may be interpolation (such as in FEM) or least-squares-based (such as in GFDM).

3.2.1. Generalized Lagrange basis functions

Definition 1. A set of functions $\left\{\phi_j(\boldsymbol{x}) \mid 1 \leq j \leq m\right\}$ form a set of *generalized Lagrange basis functions* of *degree-p consistency* over local support Ω_i with a *stencil* $\{\boldsymbol{x}_j \in \mathbb{R}^d \mid 1 \leq j \leq m\}$ if

$$\left\| \sum_{j=1}^{m} u(\boldsymbol{x}) \nabla^k \phi_j(\boldsymbol{x}) - \nabla^k u(\boldsymbol{x}) \right\|_{L^\infty(\Omega_i)} = \left\|\nabla^{p+1} u\right\|_{L^\infty(\Omega_i)} \mathcal{O}(h^{p+1-k}) \tag{3.4}$$

for a sufficiently differentiable function $u : \Omega \to \mathbb{R}$ and $k = 0, \ldots, p$, where h is the radius of the stencil. These basis functions are *stable* over Ω_i if $\left\|h^k \nabla^k \phi_j(\boldsymbol{x})\right\|_{L^\infty(\Omega_i)} \leq C \ll \infty$ for $k = 1, \ldots, p$.

In the above, the "radius" is a local length measure of the stencil, and it can be replaced by other characteristic length measures, such as the maximum distance between the points in the stencil. This definition preserves two fundamental properties of degree-p Lagrange basis functions: when approximating a function u, the coefficient for each ϕ_j is $u(\boldsymbol{x}_j)$, and u is approximated to $\mathcal{O}(h^{p+1})$ consistency. In FEM, consistent Lagrange trial (or test) functions constitute a set of generalized Lagrange basis functions.

3.2.2. Generalized Lagrange polynomials

In GFDM, the derivatives are approximated using polynomials constructed using least squares approximations. We can express them in terms of *generalized Lagrange polynomial* (*GLP*) basis functions.

Definition 2. Given a *stencil* $\{\boldsymbol{x}_j \in \mathbb{R}^d \mid 1 \leq j \leq m\}$, degree-$p$ polynomials $\left\{\phi_j(\boldsymbol{x}) \mid 1 \leq j \leq m\right\}$ form a set of *generalized Lagrange polynomial (GLP) basis functions* if every degree-p polynomial $P(\boldsymbol{x})$ is interpolated exactly by $\sum_{j=1}^m P\left(\boldsymbol{x}_j\right) \phi_j(\boldsymbol{x})$.

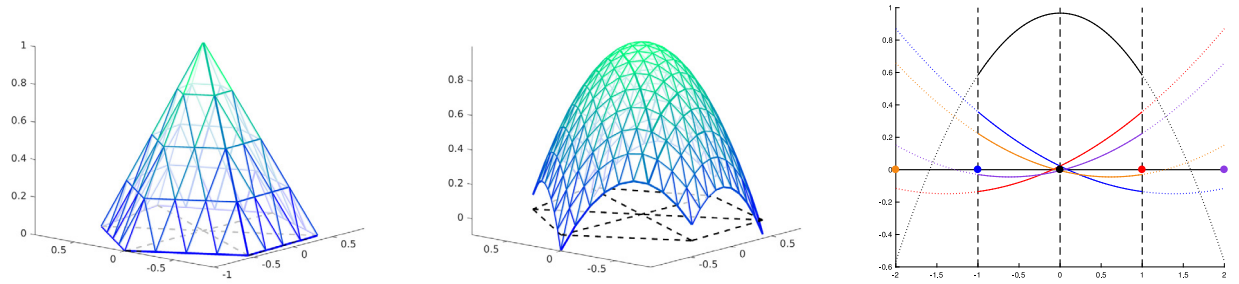

(a) A piecewise linear Lagrange basis function in 2D.

(b) A quadratic GLP basis function in 2D.

(c) A set of quadratic GLP basis functions in 1D.

Fig. 1. Piecewise Lagrange basis functions versus quadratic GLP basis functions. The basis functions in (a) and (b) are associated with the center node and have the same stencils. The basis functions in (c) form a set of five quadratic basis functions for the center node in 1D.

In practice, the GLP basis functions are computed from the pseudoinverse solution of a Vandermonde system; see e.g. [12]. For completeness, we describe the procedure in Appendix A. If the Vandermonde matrix is nonsingular, i.e., the number of points in the stencil is equal to the number of monomials of up to degree p and the stencil is not degenerate, then a set of GLP basis functions reduces to a set of Lagrange polynomial basis functions, which are commonly used in the classical finite difference methods. The basis functions are stable if the Vandermonde matrix is well conditioned. More importantly, they are generalized Lagrange trial functions.

The GLP basis functions are not unique in general in that they depend on how different points are weighted. For the AES-FEM results in Section 6, we use an inverse-distance-based weighting scheme given in (A.4). This weighting scheme tends to promote error cancellations on nearly symmetric meshes [36] and in turn improves accuracy [37]. We defer a detailed analysis to future work.

Lemma 1. *Given a set of stable degree-p GLP basis functions* $\left\{\phi_j(\boldsymbol{x}) \mid 1 \le j \le m\right\}$ *over* $\{\boldsymbol{x}_j\}$*, if u is continuously differentiable up to pth order, then* (3.4) *holds.*

Proof. Consider the d-dimensional Taylor series [38]

$$u(\boldsymbol{x}_0+\boldsymbol{h}) = \sum_{k=0}^{p} \frac{1}{k!} \nabla^k u(\boldsymbol{x}_0) : \boldsymbol{h}^k + \frac{C \left\| \nabla^{p+1} u(\boldsymbol{x}_0+\boldsymbol{\xi}) \right\|}{(p+1)!} \|\boldsymbol{h}\|^{p+1}, \tag{3.5}$$

where $\boldsymbol{h}^k$ denotes the kth tensor power of $\boldsymbol{h}$, ":" denotes the scalar product of kth-order tensors, $\|\boldsymbol{\xi}\| \le \|\boldsymbol{h}\|$, and $|C| \le 1$. Let u_p denote the degree-p Taylor polynomial (i.e., the first term in (3.5)). By definition, $u_p = \sum_{j=1}^{m} u_p\left(\boldsymbol{x}_j\right) \phi_j(\boldsymbol{x})$. Let $\delta u = u_p - u$.

$$\left\| \sum_{j=1}^{m} u\left(\boldsymbol{x}_j\right) \nabla^k \phi_j - \nabla^k u \right\|_\infty \le \left\| \sum_{j=1}^{m} \delta u\left(\boldsymbol{x}_j\right) \nabla^k \phi_j \right\|_\infty + \left\| \nabla^k \delta u \right\|_\infty, \tag{3.6}$$

where both terms are bounded by $\left\| \nabla^{p+1} u(\boldsymbol{x}) \right\|_\infty \mathcal{O}\left(h^{p-k+1}\right)$.

We note that there are some differences between the Lagrange basis functions in FEM and the GLP basis functions. First, the GLP basis functions are least-squares based, so they, in general, do not satisfy the Kronecker delta property, i.e., $\phi_j(\boldsymbol{x}_i) \ne \delta_{ij}$. Second, the Lagrange basis functions in FEM are C^0 *continuous*, whereas the GLP basis functions are *quasicontinuous* in that they are smooth over the local support, but they do not vanish exactly along the boundary. We illustrate these differences in Fig. 1, which shows (a) a 2D FEM hat function, (b) a 2D quadratic GLP basis function at a node over the same stencil, and (c) a set of GLP basis functions at a node in 1D. Third, Lagrange basis functions in FEM are defined based on a mapping between the reference domain to the physical domain, and hence they depend on element shapes and are in general not polynomials with nonlinear geometric realizations, whereas the GLP basis functions do not depend on the element shapes and are true polynomials. Finally, the GLP basis functions are defined locally at a node (or a center point), and they do not necessarily define a global set of trial functions over Ω_h. For these reasons, GWR requires a more general variational form than that used in FEM.

3.3. Component 3: Generalized variational form

Consider a node $\boldsymbol{x}_i \in \Omega_h^\circ \cup \Gamma_{h,N}^\circ$, and let ψ_i denote the test function associated with $\boldsymbol{x}_i$. Let $\boldsymbol{\Phi}_i$ denote the vector containing the trial functions $\{\phi_{ij}\}$ associated with the node $\boldsymbol{x}_i$. Let $\boldsymbol{\Phi}_{i,\circ}$ and $\boldsymbol{\Phi}_{i,D}$ denote the subvectors of $\boldsymbol{\Phi}_i$ corresponding

to the nodes in $\Omega_h^\circ \cup \Gamma_{h,N}^\circ$ and $\Gamma_{h,D}$, respectively, i.e., $\boldsymbol{\Phi}_{i,\circ} = \boldsymbol{\Phi}_{i,1:n}$ and $\boldsymbol{\Phi}_{i,D} = \boldsymbol{\Phi}_{i,n+1:m}$ in MATLAB-style colon-notation. Let $\boldsymbol{u}_h$ and $\boldsymbol{u}_D$ be composed of the nodal values associated with $\boldsymbol{\Phi}_{i,\circ}$ and $\boldsymbol{\Phi}_{i,D}$, respectively. In GWR, we approximate the solution of (2.2) locally about $\boldsymbol{x}_i$ by

$$u_{h,i} = \boldsymbol{\Phi}_i^T \begin{bmatrix} \boldsymbol{u}_h \\ \boldsymbol{u}_D \end{bmatrix} = \boldsymbol{\Phi}_{i,\circ}^T \boldsymbol{u}_h + \boldsymbol{\Phi}_{i,D}^T \boldsymbol{u}_D. \tag{3.7}$$

Let us first consider a BVP with Dirichlet boundary conditions. We define a *generalized variational form* (GVF) corresponding to (2.2) for an interior node $\boldsymbol{x}_i \in \Omega_h^\circ$ as

$$a_\circ\left(u_{h,i}, \psi_i\right) = \langle f, \psi_i \rangle_{\Omega_h}, \tag{3.8}$$

where

$$a_\circ\left(u_{h,i}, \psi_i\right) = \left\langle \mathcal{L} u_{h,i}, \psi_i \right\rangle_{\Omega_h}, \tag{3.9}$$

is the *generalized bilinear form* associated with ψ_i. Here, the inner product is computed over the local support Ω_i of ψ_i. These forms are "generalized" in that ψ_i may be a generalized function (such as a Dirac delta function). Note that if ψ_i vanishes along Γ, the bilinear form in (2.9) and the generalized bilinear form (3.9) are mathematically equivalent to each other due to Green's identities. Computationally, however, (2.9) requires ψ_i to be at least C^0 and (3.9) requires $u_{h,i}$ to be at least C^1.

3.3.1. Generalized variational form of GFDM

In (G)FDM, since the test functions are Dirac delta functions, which are not C^0, we must use (3.9) instead of (2.9) computationally. Neumann boundary conditions can be incorporated into the generalized variational form; see [1, p. 31] for derivations of second-order FDM in 1D. Alternatively, one-sided differences can be used to convert (2.4) directly into an algebraic equation at each Neumann node [1, p. 32].

3.3.2. Variational form of Lagrange FEM

For a Lagrange FEM with strongly imposed Dirichlet boundary conditions, its variational form is also a GVF. Since the trial functions are C^0, we must use the bilinear form (2.9) computationally for $\boldsymbol{x}_i \in \Omega_h^\circ$. For a BVP with Neumann boundary conditions, assuming accurate geometry, one can substitute $g_N \approx \mu \partial_{\boldsymbol{n}} u_h$ into (2.8) for each node $\boldsymbol{x}_i$ in $\Gamma_{h,N}$, which *weakly* imposes Neumann boundary conditions (2.4).

3.4. Adaptive Extended Stencil FEM

Adaptive Extended Stencil FEM or *AES-FEM*, is a GWR method that combines the features of GFDM and FEM. In particular, AES-FEM uses a piecewise linear FEM mesh, and its associated hat functions as test functions in the interior. Its trial functions are the GLP trial functions. We say that an AES-FEM is degree-p if its trial functions are degree-p GLP basis functions at each node (or more generally, at each point). Because of the least-squares nature of GLP basis functions, the number of nodes in the stencil can be chosen adaptively to ensure the well-conditioning of the Vandermonde matrix. This is the reason for the name "adaptive extended stencil" in AES-FEM; we describe the selection of the stencils and its adaptation in Appendix B. Because the test functions are C^0 and the trial functions are differentiable to pth order, we can use either (2.9) or (3.9) computationally, which would give the same results up to machine precision.

In [12], the authors considered quadratic AES-FEM and showed its second-order accuracy with Dirichlet boundary conditions. The focus of this work is to establish the well-posedness and convergence of higher-degree AES-FEM for Neumann boundary conditions over polygonal domains. As in FEM, we can substitute $g_N = \mu \partial_{\boldsymbol{n}} u_h$ into (2.8) for each node $\boldsymbol{x}_i$ in $\Gamma_{h,N}$ for AES-FEM. For curved domains, Neumann boundary conditions can be imposed using higher-order boundary representations similar to [39], as described in Section 3.1.4, or using Dirac delta test functions and one-sided differences as in GFDM. In this work, we assume polygonal domains and impose Neumann boundary conditions weakly as in FEM. We defer the analysis and comparison of different techniques for imposing Neumann conditions over curved boundaries to future work.

Remark 2. GFDM requires a cloud of nodes, rather than a mesh with elements, so it is considered a meshless method. However, to construct the stencils (a.k.a. stars), one needs a data structure, such as a quadtree/octree [40]. Because AES-FEM involves integration (see Appendix C), we use a mesh and an associated data structure to construct the stencils and to provide the elements for integration. The use of integration allows AES-FEM to enjoy additional error cancellation and hence better accuracy than GFDM on nearly symmetric meshes, as demonstrated in Section 6.

4. Well-posedness in ℓ^p norm

We first establish the *well-posedness*, and more precisely, *algebraic invertibility*, of generalized weighted residual methods for elliptic BVPs. Like that of FEM [41], this invertibility implies the existence and uniqueness of a solution in exact arithmetic. We focus on AES-FEM while making the analysis general enough for GFDM. In Section 5, we will establish the convergence of AES-FEM in the presence of rounding errors.

4.1. Algebraic equations of GWR

To analyze a GWR method, we first convert its GVF into a system of linear equations. For generality, we assume the bilinear form (2.9), with strongly imposed Dirichlet boundary conditions and weakly imposed Neumann boundary conditions. For GFDM, we assume only Dirichlet boundary conditions, and the GVF is evaluated with (3.9) instead of (2.9).

From (2.9), we obtain an $n \times n$ linear system in $\boldsymbol{u}_h$, namely,

$$\boldsymbol{A}\boldsymbol{u}_h = \boldsymbol{b}, \tag{4.1}$$

where the ith row of $\boldsymbol{A}$ and $\boldsymbol{b}$ are

$$\boldsymbol{a}_i^T = a(\boldsymbol{\Phi}_{i,\circ}^T, \psi_i), \tag{4.2}$$

$$b_i = \langle f, \psi_i \rangle_{\Omega_h} - a\left(\boldsymbol{\Phi}_{i,D}^T \boldsymbol{u}_D, \psi_i\right) + \langle \mu \partial_{\boldsymbol{n}} u_h, \psi_i \rangle_{\Gamma_{h,N}}, \tag{4.3}$$

respectively. For the Poisson equation, $\boldsymbol{A}$ is the *stiffness matrix* and $\boldsymbol{b}$ is the *load vector* in FEM. For generality, we simply refer to $\boldsymbol{A}$ as the *coefficient matrix*. Another important matrix is the *mass matrix*, which is the coefficient matrix of the *constrained projection* associated with the GWR,

$$\boldsymbol{M}\boldsymbol{u}_P = \boldsymbol{b}_P, \tag{4.4}$$

where the ith row of $\boldsymbol{M}$ and $\boldsymbol{b}$ are

$$\boldsymbol{m}_i^T = \langle \boldsymbol{\Phi}_{i,\circ}^T, \psi_i \rangle_{\Omega_h},$$
$$b_{P,i} = \left\langle u - u_D \boldsymbol{\Phi}_{i,D}^T \boldsymbol{u}_D, \psi_i \right\rangle_{\Omega_h}.$$

For Galerkin FEM, the constrained projection is known as the L^2 *projection* [41, p. 132]. Note that Neumann constraints are not imposed explicitly in the constrained projection because they are satisfied weakly automatically.

4.2. Algebraic error analysis in ℓ^p norm

To analyze the solutions of (4.1), we consider the nodal values in ℓ^p norm. Given a vector $\boldsymbol{v} \in \mathbb{R}^n$, its ℓ^p norm is $\|\boldsymbol{v}\|_p = \sqrt[p]{\sum_{i=1}^n |v_i^p|}$, where $1 \le p \le \infty$. Note that this p is independent of, and different from, the degree of the basis functions. We will primarily use the ℓ^2 or ℓ^∞ norm (i.e., $p = 2$ or $p = \infty$). The ℓ^p *norm* of $\boldsymbol{A} \in \mathbb{R}^{n\times n}$ is $\|\boldsymbol{A}\|_p = \sup_{\|\boldsymbol{v}\|_p=1} \|\boldsymbol{A}\boldsymbol{v}\|_p$.

Let $\boldsymbol{u}_h \in \mathbb{R}^n$ denote the solution vector of a GWR method on a mesh with n nodes. Let $\boldsymbol{u}_I$ denote the vector composed of $u(\boldsymbol{x}_i)$. The *error vector* is

$$\delta\boldsymbol{u} = \boldsymbol{u}_h - \boldsymbol{u}_I. \tag{4.5}$$

Consider the linear system (4.1). Its *residual vector* is

$$\boldsymbol{r} = \boldsymbol{b} - \boldsymbol{A}\boldsymbol{u}_I = \boldsymbol{A}(\boldsymbol{u}_h - \boldsymbol{u}_I) = \boldsymbol{A}\delta\boldsymbol{u}. \tag{4.6}$$

Suppose $\boldsymbol{A} \in \mathbb{R}^{n\times n}$ is nonsingular, and assume exact arithmetic. Then,

$$\|\delta\boldsymbol{u}\|_p \le \left\|\boldsymbol{A}^{-1}\right\|_p \|\boldsymbol{r}\|_p, \tag{4.7}$$

where $\left\|\boldsymbol{A}^{-1}\right\|_p$ is the *absolute condition number in p-norm* of the linear system (4.1). Note that given $\boldsymbol{A} \in \mathbb{R}^{n\times n}$ and $\boldsymbol{B} \in \mathbb{R}^{n\times n}$, $\|\boldsymbol{A}\boldsymbol{B}\|_p \le \|\boldsymbol{A}\|_p \|\boldsymbol{B}\|_p$.

4.3. Well-posedness of constrained projection in ℓ^p norm

We first apply backward error analysis to the constrained projection (4.4). It is an important base case for the analysis of elliptic PDEs. In particular, consider a perturbation δu to u in the right-hand side of (4.4). This leads to a perturbation $\delta\boldsymbol{b}$ in $\boldsymbol{b}_P$. From (4.7), the perturbation $\delta\boldsymbol{u}$ in $\boldsymbol{u}_P$ is bounded by

$$\|\delta\boldsymbol{u}\|_p \le \left\|\boldsymbol{M}^{-1}\right\|_p \|\delta\boldsymbol{b}\|_p. \tag{4.8}$$

If δu is C^0 continuous, $\|\delta\boldsymbol{b}\|_p = (1 + \mathcal{O}(h)) \|\boldsymbol{M}\, [\![\delta u(\boldsymbol{x}_i)]\!]\|_p \le \mathcal{O}(1) \|\boldsymbol{M}\|_p \|[\![\delta u(\boldsymbol{x}_i)]\!]\|_p$, so $\|\delta\boldsymbol{u}\|_p = \mathcal{O}(1) \|[\![\delta u(\boldsymbol{x}_i)]\!]\|_p$ if $\kappa_p(\boldsymbol{M}) = \mathcal{O}(1)$; on the other hand, if $\kappa_p(\boldsymbol{M}) = \mathcal{O}(h^{-\alpha})$ for some $\alpha > 0$, an $\mathcal{O}(1)$ continuous perturbation δu in the right-hand side of (4.4) may lead to an $\mathcal{O}(h^{-\alpha})$ perturbation in $\delta\boldsymbol{u}$ in ℓ^p norm. Hence, to be consistent with the classical Hadamard's notion of well-posedness of variational methods [41, p. 82], we define a well-posed constrained projection as follows.

Definition 3. A constrained projection is *well-posed* in ℓ^p norm for $1 \leq p \leq \infty$ independently of h if it is *well-conditioned*, i.e.,

$$\kappa_p(\boldsymbol{M}) = \|\boldsymbol{M}\|_p \left\|\boldsymbol{M}^{-1}\right\|_p = \mathcal{O}(1). \tag{4.9}$$

In practice, the well-posedness requires *quasiuniform meshes*.

Definition 4. A type of GWR meshes is *quasiuniform* if the ratio of the largest and smallest control volumes of the test functions is bounded independently of mesh resolution, i.e., $\sup_i |\omega_i| / \inf_i |\omega_i| = \mathcal{O}(1)$.

For FEM, Definition 4 is satisfied with the classical definition of quasiuniform meshes (e.g., [9,3]), which requires the ratio between the largest and smallest elements to be bounded. Definition 4 is more general and also applies to GFDM, of which the control volumes have nonzero measures, but the local support of a Dirac delta function has a zero measure; see Remark 3. For AES-FEM, we note the following fact.

Theorem 2. *Constrained projection by AES-FEM is well-posed in ℓ^p norm for $1 \leq p \leq \infty$ on a sufficiently fine quasiuniform mesh with consistent and stable GLP basis functions and test functions.*

This theorem is similar to that of the well-posedness of L^2 projections [41, p. 387], but there are two complications. First, the GLP basis functions are not global basis functions over Ω_h, so we cannot use functional analysis directly. Second, Theorem 2 is not limited to ℓ^2 norms, so we cannot use eigenvalue analysis either. To address the first issue, we define a global basis function by blending the GLP basis functions using $\{\psi_i\}$ to obtain a C^0 basis function, i.e., $\hat{\boldsymbol{\Phi}} = \sum_{i=1}^{m} \psi_i \boldsymbol{\Phi}_i$, which is composed of

$$\hat{\phi}_j = \sum_{i=1}^{n} \psi_i \phi_{ij}. \tag{4.10}$$

These blended basis functions have the same approximation order as the GLP basis functions [42], and hence

$$\left|\hat{\boldsymbol{v}}^T \boldsymbol{M} \hat{\boldsymbol{u}}\right| = \left\langle \hat{\boldsymbol{\Phi}}^T \hat{\boldsymbol{u}},\ \boldsymbol{\Psi}^T \hat{\boldsymbol{v}} \right\rangle \left(1 + \mathcal{O}\left(h^{p+1}\right)\right). \tag{4.11}$$

To overcome the second issue, we make use of Singer's representation theorem [43]. We omit the detailed proof, which is similar to that of Theorem 3 below.

4.4. Well-posedness for elliptic BVPs

Consider a perturbation δf to f in the right-hand side of (4.4). This leads to a perturbation $\delta \boldsymbol{b}$ in $\boldsymbol{b}_P$, where $n^{-\frac{1}{p}} \|\delta \boldsymbol{b}\|_p \leq \|\boldsymbol{M}\|_p \|\delta f\|_\infty$. From (4.7), the perturbation $\delta \boldsymbol{u}$ in $\boldsymbol{u}_h$ is bounded by

$$\|\delta \boldsymbol{u}\|_p \leq \left\|\boldsymbol{A}^{-1}\right\|_p \|\delta \boldsymbol{b}\|_p. \tag{4.12}$$

Hence, $n^{-\frac{1}{p}} \|\delta \boldsymbol{u}\|_p = \mathcal{O}(1) \|\delta f\|_\infty$ if $\left\|\boldsymbol{A}^{-1}\right\|_p \|\boldsymbol{M}\|_p = \mathcal{O}(1)$. On the other hand, if $\left\|\boldsymbol{A}^{-1}\right\|_p \|\boldsymbol{M}\|_p = \mathcal{O}(h^{-\alpha})$ for some $\alpha > 0$, an $\mathcal{O}(1)$ C^0 continuous perturbation δf in the right-hand side of (4.4) may lead to an $\mathcal{O}(h^{-\alpha})$ perturbation in $\delta \boldsymbol{u}$ in $\boldsymbol{u}_h$. Hence, we define well-posedness as follows.

Definition 5. Given an elliptic BVP, let $\boldsymbol{A}$ and $\boldsymbol{M}$ denote the coefficient and mass matrices defined in (4.1) and (4.4), respectively. A GWR method is *well-posed in ℓ^p norm* for $1 \leq p \leq \infty$ independently of h if

$$\left\|\boldsymbol{A}^{-1}\boldsymbol{M}\right\|_p \leq \left\|\boldsymbol{A}^{-1}\right\|_p \|\boldsymbol{M}\|_p = \mathcal{O}(1). \tag{4.13}$$

For AES-FEM, we note the following theorem.

Theorem 3. *Given an elliptic BVP, AES-FEM is well-posed in ℓ^p norm for $1 \leq p \leq \infty$ on a sufficiently fine quasiuniform mesh with consistent and stable GLP basis functions and test functions.*

Similar to Theorem 2, the proof requires an adaptation by using $\hat{\boldsymbol{\Phi}}$ to construct a C^0 approximation in order to apply Singer's representation theorem. Similar to the Lax–Milgram lemma, the proof also involves an assumption of invertibility of the PDE in infinite dimensions, and a boundedness assumption due to Friedrichs' inequality [9, p. 104], which is more general than the Poincaré inequality [41, p. 489]. For completeness, we give the proof as follows.

Proof. Let $\hat{\boldsymbol{u}} = \arg\inf_{\|\boldsymbol{u}\|_p=1} \|\boldsymbol{A}\boldsymbol{u}\|_p$ and $\hat{u} = \hat{\boldsymbol{\Phi}}^T \hat{\boldsymbol{u}}$. Let p' denote *Hölder's conjugate* of p, i.e., $1/p + 1/p' = 1$, and let $\hat{v} = \arg\sup_{\|v\|_{L^{p'}}=1} a\left(\hat{u}, v\right)_\Omega$. Since $\hat{u}$ is C^0 continuous, due to Singer's representation theorem, there exists a solution $\hat{\boldsymbol{v}}$ such that $a\left(\hat{u}, \boldsymbol{\Psi}^T \hat{\boldsymbol{v}}\right) = a\left(\hat{u}, \hat{v}\right)$. If the PDE is invertible in infinite dimensions,

$$\exists C, \qquad \inf_{\|v\|_{L^p(\Omega)}=1} \sup_{\|v\|_{L^{p'}(\Omega)}=1} a(u, v) \geq C > 0. \tag{4.14}$$

Due to Friedrichs' inequality, $\left\|\hat{u}\right\|_{L^p}\left\|\boldsymbol{\Psi}^T\hat{\boldsymbol{v}}\right\|_{L^{p'}} \leq \Theta(1)a\left(\hat{u},\hat{v}\right)$ and $\left\|\boldsymbol{\Psi}^T\hat{\boldsymbol{v}}\right\|_{L^{p'}} = \Theta(1)$. Furthermore, $\left\|\boldsymbol{A}^{-1}\right\|_p^{-1} = \sup_{\boldsymbol{v}\neq\boldsymbol{0}}\left|\boldsymbol{v}^T\boldsymbol{A}\hat{\boldsymbol{u}}\right|/\|\boldsymbol{v}\|_{p'}$, Hence,

$$\left\|\hat{\boldsymbol{v}}\right\|_{p'}\left\|\boldsymbol{A}^{-1}\right\|_p^{-1} \geq \left|\hat{\boldsymbol{v}}^T\boldsymbol{A}\hat{\boldsymbol{u}}\right| = a\left(\hat{u},\hat{v}\right)(1+\mathcal{O}(h)) \geq (C+\mathcal{O}(h))\left\|\hat{u}\right\|_{L^p}. \tag{4.15}$$

On a quasiuniform mesh,

$$\left\|\hat{u}\right\|_{L^p} = \left(\sum_{i=1}^m \int_{\omega_i} |\hat{u}|^p \, d\boldsymbol{x}\right)^{1/p} = \Theta(1)\left(\max|\omega_i|\right)^{1/p}. \tag{4.16}$$

Since $\left\|\hat{v}\right\|_{L^{p'}} = 1$,

$$\left\|\hat{\boldsymbol{v}}\right\|_{p'} = \left(\sum_{i=1}^m \left|\hat{v}_i\right|^{p'}\right)^{1/p'} \leq \frac{\left(\sum_{i=1}^m \left|\hat{v}_i^{p'}\,|\omega_i|\right|\right)^{1/p'}}{\left(\min|\omega_i|\right)^{1/p'}} = \frac{\left\|\boldsymbol{\Psi}^T\hat{\boldsymbol{v}}\right\|_{L^{p'}} + \mathcal{O}(h)}{\left(\min|\omega_i|\right)^{1/p'}}. \tag{4.17}$$

Since $\|\boldsymbol{M}\|_p = \max|\omega_i|\,\Theta(1) = \min|\omega_i|\,\Theta(1)$,

$$\left\|\hat{\boldsymbol{v}}\right\|_{p'}/\left\|\hat{u}\right\|_{L^p} \leq \Theta(1)\left(\min|\omega_i|\right)^{-1/p-1/p'} = \Theta(1)\|\boldsymbol{M}\|_p^{-1}, \tag{4.18}$$

and

$$\left\|\boldsymbol{A}^{-1}\boldsymbol{M}\right\|_p \leq \|\boldsymbol{M}\|_p\left\|\boldsymbol{A}^{-1}\right\|_p = \frac{\|\boldsymbol{M}\|_p\left\|\hat{\boldsymbol{v}}\right\|_{p'}}{\left|\hat{\boldsymbol{u}}\boldsymbol{A}\hat{\boldsymbol{v}}\right|} \leq \frac{\|\boldsymbol{M}\|_p\left\|\hat{\boldsymbol{v}}\right\|_{p'}}{(C+\mathcal{O}(h))\left\|\hat{u}\right\|_{L^p}} = \mathcal{O}(1). \tag{4.19}$$

Let $\delta\boldsymbol{u}_{h-l} = \boldsymbol{u}_h - \boldsymbol{u}_l$, where $\boldsymbol{u}_h$ is composed of nodal solutions of AES-FEM and $\boldsymbol{u}_l$ is composed of the interpolated nodal values. It is easy to see that the above proof also applies to FEM, simply by replacing $\hat{\boldsymbol{\Phi}}$ with the Lagrange basis functions $\boldsymbol{\Phi}$ in the proof. Hence, Theorems 2 and 3 both apply to FEM.

Remark 3. We can generalize Theorems 2 and 3 to GFDM as follows. Let $\hat{\boldsymbol{M}} = \boldsymbol{W}\boldsymbol{M}$ and $\hat{\boldsymbol{A}} = \boldsymbol{W}\boldsymbol{A}$, where $\boldsymbol{W}$ is a diagonal matrix with $w_i = |\omega_i|$. Let $\hat{\boldsymbol{\Psi}}$ denote the vector of hat functions over the mesh. Then, it is easy to show that $\left|\hat{\boldsymbol{v}}^T\hat{\boldsymbol{M}}\hat{\boldsymbol{u}}\right| = \left\langle\hat{\boldsymbol{\Phi}}^T\hat{\boldsymbol{u}},\hat{\boldsymbol{\Psi}}^T\hat{\boldsymbol{v}}\right\rangle(1+\mathcal{O}(h))$ and $\left|\hat{\boldsymbol{v}}^T\hat{\boldsymbol{A}}\hat{\boldsymbol{u}}\right| = a\left(\hat{\boldsymbol{\Phi}}^T\hat{\boldsymbol{u}},\hat{\boldsymbol{\Psi}}^T\hat{\boldsymbol{v}}\right)(1+\mathcal{O}(h))$. By replacing $\boldsymbol{A}$ with $\hat{\boldsymbol{A}}$, the proof for Theorem 3 applies to GFDM with Dirichlet boundary conditions; similarly for Theorem 2.

Note that $\|\boldsymbol{A}\|_p = \|\boldsymbol{M}\|_p\mathcal{O}(h^{-2})$ on a quasiuniform mesh with stable GLP basis functions. Hence a corollary of Theorem 3 is that

$$\kappa_p(\boldsymbol{A}) = \|\boldsymbol{A}\|_p\left\|\boldsymbol{A}^{-1}\right\|_p \leq \|\boldsymbol{M}\|_p\left\|\boldsymbol{A}^{-1}\right\|_p\mathcal{O}(h^{-2}) = \mathcal{O}(h^{-2}) \tag{4.20}$$

on a quasiuniform mesh. Similarly, $\kappa_p(\boldsymbol{M}^{-1}\boldsymbol{A}) = \mathcal{O}(h^{-2})$. This condition number estimation is well known in ℓ^2 norm for FDM and FEM (see e.g. [41,1]).

4.5. Mesh dependency for well-posedness

From the preceding analysis, it is clear that all the GWR methods have some level of dependency on meshes. In particular, all the methods require the *quasiuniformity* of control volumes of the nodes. For FEM and AES-FEM, this is equivalent to the quasiuniformity of the local support of the test functions. For GFDM, although the computation does not depend on a mesh, the quasiuniformity imposes restrictions on the distributions of the nodes.

Besides quasiuniformity, FEM requires *well-shaped* elements, because the Lagrange trial and test functions are based on the transformation from the parametric space to the physical space. For linear elements over polytopal domains, the well-shapedness requires the angles within the elements to be bounded away from π and 0 [44,45], which is needed for the stability of interpolations and derivative approximations. If some elements contain angles that are too small, the stiffness matrix in FEM may become ill-conditioned [46]. For high-order elements, the nodes must be well-positioned within the master elements so that the Lagrange basis functions are stable. In contrast, the well-posedness of GFDM does not depend on element shapes, but the stability of the GLP basis functions does depend on the selection of the stencils. Similarly, AES-FEM also depends on the stencils for the stability of its trial functions. However, the stencils in GFDM and AES-FEM can be adapted more easily due to their least squares nature. If the generalized bilinear form (3.9) is used, then AES-FEM also depends on the stability of the Lagrange test functions in the parametric space, but it does not require well-shaped elements in the physical space. If the bilinear form (2.9) is used over linear elements, then (2.9) is equal to (3.9) to machine precision, and hence there is no dependency on element shape either. In addition, high-order AES-FEM requires only first-order meshes for its implementation at least in the interior of the domain, so its implementation is simpler than that of high-order finite elements, which requires high-order meshes.

For geometries with curved boundaries, Lagrange FEM typically uses isoparametric elements, for which the well-posedness depends on the Ciarlet–Raviart condition [35]. Assuming stable Lagrange basis functions, the Ciarlet–Raviart condition requires the kth derivatives for the mapping from the physical space to the parametric space to be bounded for $k = 2, \ldots, p+1$, i.e., $h^k \left\| \nabla_{\boldsymbol{x}}^k \boldsymbol{\xi} \right\|_\infty \leq C \ll \infty$ for $\boldsymbol{\xi}$ in the master element. Mathematically, this condition is needed due to the high-order chain rule, also known as the Faà di Bruno's formula [47],

$$\partial_{\boldsymbol{d}}^k \phi\left(\boldsymbol{\xi}(\boldsymbol{x}_0)\right) = \sum_{m_i \geq 0}^{m_1+2m_2+\cdots+km_k=k} \frac{k!}{\boldsymbol{m}!} \nabla_{\boldsymbol{\xi}}^{|\boldsymbol{m}|} \phi(\boldsymbol{\xi}) : \prod_{i=1}^{k} \left(\frac{\partial_{\boldsymbol{d}}^i \boldsymbol{\xi}(\boldsymbol{x}_0)}{i!} \right)^{m_i}, \tag{4.21}$$

where $\boldsymbol{m} = [m_1, \ldots, m_k]$, $\boldsymbol{m}! = \prod_{i=1}^k m_i!$, $|\boldsymbol{m}| = \sum_{i=1}^k m_i$, $\nabla_{\boldsymbol{\xi}}^{|\boldsymbol{m}|}$ denotes the derivative tensor of order $|\boldsymbol{m}|$, and ":" denotes the scalar product of kth-order tensors. For AES-FEM, if (3.9) is used with a higher-order boundary representation, then the Ciarlet–Raviart condition is also required when computing $\nabla \psi_i$. However, the generalized bilinear form (3.9) uses only $\psi_i(\boldsymbol{\xi})$ over the master element, so the Ciarlet–Raviart condition is no longer required. In this case, however, AES-FEM requires imposing Neumann boundary conditions similar to the techniques in GFDM instead of FEM. The well-posedness and consistency of such a hybrid treatment over curved boundaries require a more general analysis, and we defer it to future work.

5. Convergence in ℓ^p norm

In this section, we analyze the convergence of GWR methods in ℓ^p norm. Given a vector of nodal errors $\delta \boldsymbol{u}$, the *convergence rate in ℓ^p norm* is kth order if $\|\delta \boldsymbol{u}\|_p = \sqrt[p]{n}\mathcal{O}(h^k)$, where h is some edge length measure of a quasiuniform mesh.

5.1. Convergence of GWR methods for constrained projection

Let $\delta \boldsymbol{u}_{P-I} = \boldsymbol{u}_P - \boldsymbol{u}_I$, where $\boldsymbol{u}_P$ and $\boldsymbol{u}_I$ are the projected and interpolated nodal values. We then obtain the following result regarding the convergence of the constrained projection.

Theorem 4 (*Convergence of Constrained Projection*)**.** *Under the same assumptions as in Theorem 2, if u is continuously differentiable to pth order within each element, the solution of the constrained projection with a well-posed degree-p GWR method converges at $\mathcal{O}(h^{p+1})$ or better in ℓ^∞ norm, i.e., $\|\delta \boldsymbol{u}_{P-I}\|_\infty \leq \mathcal{O}(h^{p+1})$.*

Proof. Let $\boldsymbol{r} = \left\langle u - u_I,\ \boldsymbol{\Psi}_{\circ;N} \right\rangle_\Omega$. Due to the consistency of GLP basis functions, $\|\boldsymbol{r}\|_\infty \leq \|\boldsymbol{M}\|_\infty \mathcal{O}(h^{p+1})$, so

$$\|\delta \boldsymbol{u}_{P-I}\|_\infty \leq \left\|\boldsymbol{M}^{-1}\right\|_\infty \|\boldsymbol{r}\|_\infty \leq \left\|\boldsymbol{M}^{-1}\right\|_\infty \|\boldsymbol{M}\|_\infty \mathcal{O}(h^{p+1}) = \mathcal{O}(h^{p+1}). \tag{5.1}$$

The theorem also applies to other ℓ^p norms. In Theorem 4, we use "$\leq$" sign to emphasize that the bound may not be tight due to possible superconvergence. Note that Theorem 4 applies to FEM, GFDM, and AES-FEM. For all of these methods, if p is even, the leading error term in the residual $\boldsymbol{r}$ is odd order, which may cancel out in the integration. In turn, it may lead to superconvergence. The superconvergence of FEM for the L^2 projection was considered in [48].

5.2. Convergence of GWR methods for elliptic BVPs

Let $\boldsymbol{u}_h$ denote the nodal solutions of (4.1) corresponding to the nodes in $\Omega_h^\circ \cup \Gamma_{h,N}^\circ$. Let $\delta \boldsymbol{u}_{h-I} = \boldsymbol{u}_h - \boldsymbol{u}_I$. We first give a loose error bound using an argument similar to that of Theorem 4. We state the bound in ℓ^∞ norm, but the result also holds in any ℓ^p norm for $1 \leq p \leq \infty$.

Lemma 5. *Under the same assumptions as in Theorem 3, assuming exact arithmetic, the solution with a well-posed degree-p GWR method for an elliptic BVP converges at $\mathcal{O}(h^{p-1})$ or better in ℓ^∞ norm, i.e., $\|\delta \boldsymbol{u}_{h-I}\|_\infty \leq \mathcal{O}(h^{p-1})$.*

Proof. Let $\boldsymbol{r} = a(u - u_I,\ \boldsymbol{\Psi}_{\circ,N})$. Using the same argument as for Lemma 1, it is easy to show that $\left\| \mathcal{L} \boldsymbol{\Phi}_i^T \delta \boldsymbol{u}_{h-I} \right\|_\infty = \mathcal{O}(h^{p-1})$ for $\boldsymbol{x}_i \in \Omega_h$. Hence, $\|\boldsymbol{r}\|_\infty \leq \|\boldsymbol{M}\|_\infty \mathcal{O}(h^{p-1})$, and

$$\|\delta \boldsymbol{u}_{h-I}\|_\infty \leq \left\|\boldsymbol{A}^{-1}\right\|_\infty \|\boldsymbol{r}\|_\infty \leq \left\|\boldsymbol{A}^{-1}\right\|_\infty \|\boldsymbol{M}\|_\infty \mathcal{O}(h^{p-1}) = \mathcal{O}(h^{p-1}). \tag{5.2}$$

Remark 4. Lemma 5 assumes exact arithmetic. This is important because in the presence of approximation or rounding errors, the solutions may not converge due to *ill-conditioning*; see e.g. [1, p. 45] for finite differences and [41, p. 222] for finite elements.

For FEM, Lemma 5 underestimates the convergence rate by two orders, compared to the well-known $\mathcal{O}(h^{p+1})$ error bounds in L^2 norm due to the Aubin–Nitsche duality argument; see e.g. [3]. The derivation of error bounds for FEM in ℓ^p norm is beyond the scope of this work. For GFDM and AES-FEM, however, the Aubin–Nitsche duality argument does not apply, due to the non-conformity. For odd-degree-p GFDM and AES-FEM, Lemma 5 is tight. However, for even-degree-p, similar to constrained projections, the leading error term in the residual $\boldsymbol{r}$ is odd order, which may cancel out in the integration. For GFDM, this error cancellation occurs with symmetric stencils, analogous to centered differences, leading to $\mathcal{O}(h^p)$ convergence rate. With AES-FEM, however, the error cancellation is primarily due to the numerical integration, for example, see Fig. 4.

Theorem 6. *Under the same assumptions as in Theorem 3, assuming exact arithmetic, the solution of a well-posed even-degree-p AES-FEM for a coercive elliptic BVP with Dirichlet boundary conditions converges at $\mathcal{O}(h^p)$ in ℓ^∞ norm, if $p = 2$ or if $p \geq 4$ and the local support is nearly symmetric.*

Proof. Let $u_{I,i}$ denote the local interpolation at a node $\boldsymbol{x}_i \in \Omega_h^\circ$. Let $\delta u_i = u_{I,i} - u$, which is a smooth function over Ω_i. Apply $\mathcal{L}$ to δu_i. We note that

$$\mathcal{L}\delta u_i(\boldsymbol{x}_i + \boldsymbol{h}) = C\left(\operatorname{sign}\left(\boldsymbol{h}\cdot\hat{\boldsymbol{h}}\right)\|\boldsymbol{h}\|\right)^{p-1} + \mathcal{O}(h^p), \tag{5.3}$$

where C is proportional to $\left\|\partial_{\hat{\boldsymbol{h}}}^{p+1}u(\boldsymbol{x})\right\|_\infty$. If $p = 2$, because ψ_i is the hat function, the line integral of $\left(\operatorname{sign}\left(\boldsymbol{h}\cdot\hat{\boldsymbol{h}}\right)\|\boldsymbol{h}\|\right)^{p-1}\psi_i(\boldsymbol{x}_i + \boldsymbol{h})$ cancels out exactly, so $\|\boldsymbol{r}\|_\infty \leq \|\boldsymbol{M}\|_\infty \mathcal{O}(h^2)$ in Lemma 5. For even $p \geq 4$, the line integral cancels out if the local support is (nearly) symmetric about $\boldsymbol{x}_i$.

In [12], quadratic AES-FEM was shown to converge at second order, but the proof did not explicitly state the error cancellation. Theorem 6 indicates that AES-FEM may not enjoy the full $\mathcal{O}(h^p)$ superconvergence for $p \geq 4$ on highly irregular meshes, but in practice we observe it to be close to $\mathcal{O}(h^p)$ on quasiuniform meshes, as we will demonstrate in Section 6.2.

6. Numerical results

In this section, we present some numerical results to verify the theoretical analysis in this work.

6.1. Comparison of mesh dependency

We first compare the mesh dependency of FEM to that of AES-FEM. As shown in Section 4.5, the well-posedness of FEM depends on well-shapedness of the meshes, while AES-FEM is independent of element shapes, regardless of the degree of the GLP basis functions. To demonstrate this, we solved the Poisson equation in 2D

$$-\Delta u = f \tag{6.1}$$

with Dirichlet boundary conditions over $[-1, 1]^2$. We obtained f and u_D from the exact solution $u = \cos(\pi x)\cos(\pi y)$ and solved the equation using our own implementations of quadratic, quartic, and sextic AES-FEM, along with linear, quadratic, and cubic FEM. We generated a series of meshes on a unit square with progressively worse element quality, which we obtain by distorting a good-quality mesh. For AES-FEM and linear FEM, we used a mesh with 130,288 elements and 65,655 nodes and distorted four elements by moving one vertex of each of these elements incrementally towards its opposite edge. For quadratic FEM, the mesh had 32,292 elements and 65,093 nodes, and a single element was distorted by moving one vertex and its adjacent mid-edge nodes incrementally towards its opposite edge. For cubic FEM, the mesh had 32,292 elements and 146,077 nodes, and also a single element was distorted. Fig. 2 shows the condition numbers of the stiffness matrices of FEM and AES-FEM.

In practice, the condition number may affect the efficiency of iterative solvers. Fig. 3 shows the numbers of iterations required to solve the linear systems to a relative tolerance of 10^{-8} using GMRES for AES-FEM and CG for FEM, both with Gauss–Seidel preconditioners. It can be seen that the condition numbers of FEM increased inversely proportional to the minimum angle, and the number of iterations of CG grew correspondingly. In contrast, the condition numbers and the number of iterations for AES-FEM remained constant. We observed similar behavior for 3D AES-FEM, which we omit from the paper.

6.2. Convergence of high-order AES-FEM

Next, we verify the convergence analysis in Section 5.2, especially that of AES-FEM. To this end, we used AES-FEM of degrees 2 to 6 to solve the equation

$$-\Delta u + \boldsymbol{v}\cdot\nabla u = f, \tag{6.2}$$

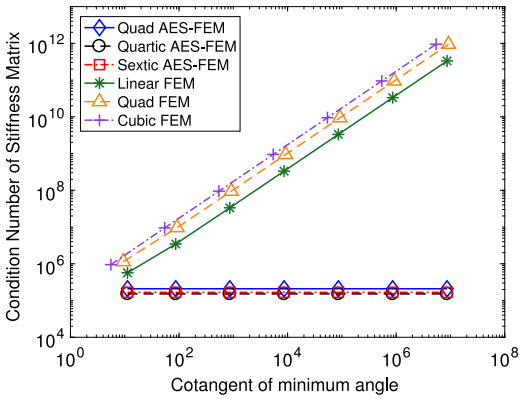

Fig. 2. Dependence of the condition numbers of the stiffness matrices of FEM and AES-FEM on the worse angles.

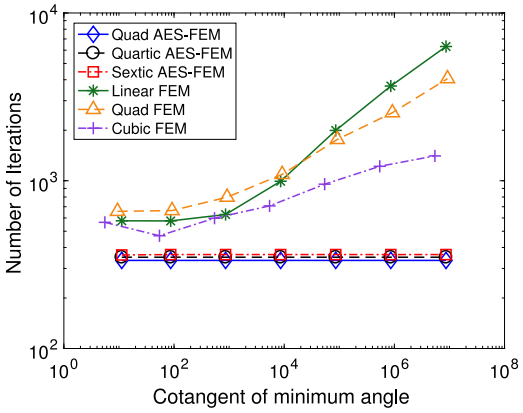

Fig. 3. Relationship of the number of iterations of the preconditioned iterative solvers and the worst angles.

with unstructured meshes over $[-1, 1]^2$, where $f = \sin \pi x \sin \pi y$. Fig. 4(a) shows the convergence rates in the relative ℓ^2 norm for the Poisson equation, for which $\boldsymbol{v} = \mathbf{0}$. Fig. 4(b) and (c) show the convergence rates for the advection–diffusion equation with Dirichlet and Neumann boundary conditions, respectively, where $\boldsymbol{v} = [x, -y]$. The number to the right of each convergence curve shows the average convergence rate under mesh refinement. Note that AES-FEM with even-degree basis functions converged at about pth order whereas with odd-degree basis functions, AES-FEM converged at $(p-1)$st order. For example, with quadratic and cubic basis functions, the convergence rate is approximately second order. This difference in convergence rates is due to error cancelation in the numerical integration, as discussed in Section 5.2.

6.3. Comparison of FEM, GFDM, and AES-FEM

Finally, we compare the accuracy of FEM, GFDM, and FEM. We use the Poisson equation in this comparison. In particular, we solved a 2D Poisson equation (6.1) over the square $[-1, 1]^2$ with an elliptical hole of semi-axes 0.5 and 0.2 in the middle. The domain, as illustrated in Fig. 5(a), has nonuniform curvature along the inner boundary and has corners along the outer boundary. We applied Neumann boundary conditions to the outer boundary and applied Dirichlet boundary conditions to the inner boundary. We obtained the source term f and the boundary conditions by differentiating the following analytic function

$$u = \sin(\pi x) \sin(\pi y) . \tag{6.3}$$

First, let us focus on comparing linear and quadratic FEM, GFDM, and AES-FEM. For FEM, we used the Partial Differential Equation (PDE) Toolbox in MATLAB R2018a [49], which supports linear and quadratic elements. Hence, we focus on comparing linear and quadratic FEM with quadratic AES-FEM and GFDM. We refer to all these methods as "low-order". We generated the meshes directly using PDE Toolbox and used the built-in solvers in MATLAB with default tolerances. The number of nodes ranged between 709 and 40,872. Fig. 5(b) compares these lower-order methods, where the number to the right of each convergence curve indicates the average convergence rates. Quadratic AES-FEM had slightly better

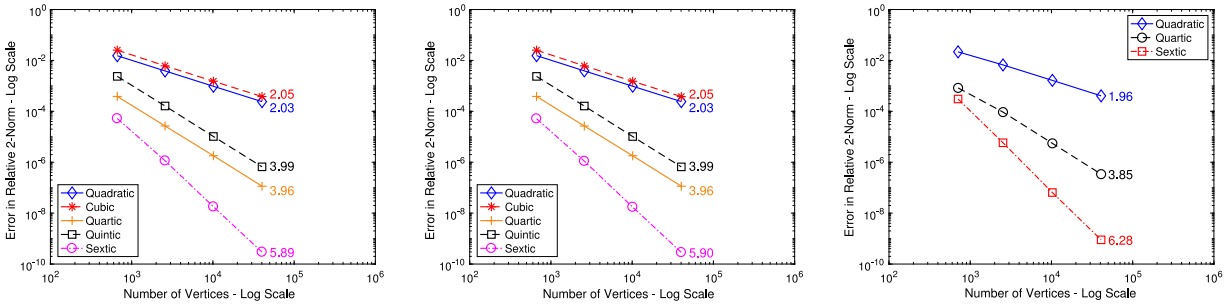

(a) Poisson equation with Dirichlet boundaries.

(b) Advection-diffusion equation with Dirichlet boundaries.

(c) Advection-diffusion equation with Neumann boundaries.

Fig. 4. The errors in the function values from AES-FEM for 2D Poisson and advection–diffusion equations. The number to the right of each curve indicates the average convergence rate.

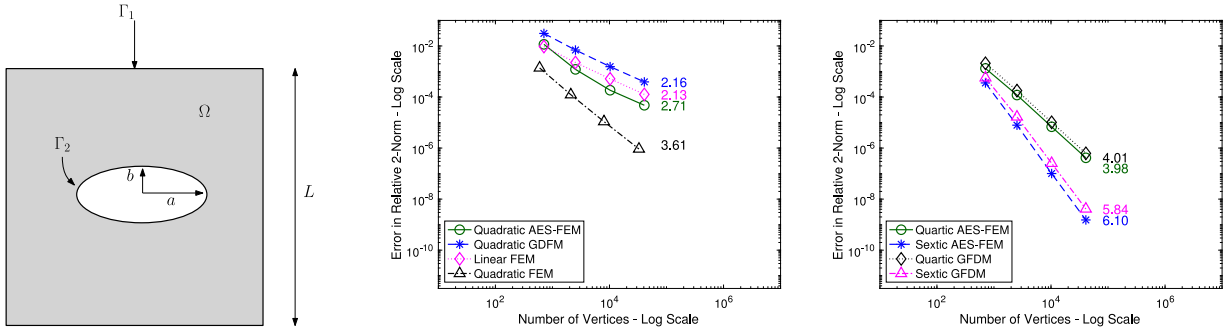

(a) Test domain.

(b) Low-order methods.

(c) High-order methods.

Fig. 5. Comparison of FEM, GFDM, and AES-FEM for the Poisson equation.

accuracy than linear FEM on finer meshes. GFDM and AES-FEM have identical sparsity patterns, but GFDM had significantly larger errors than AES-FEM.

Next, we compare quartic and sextic AES-FEM and GFDM. We used the same meshes as for quadratic AES-FEM. Fig. 5(c) compares AES-FEM and GFDM for the problem. For GFDM, we applied Neumann conditions by averaging the one-sided derivatives on both left- and right-hand sides at corners. It can be seen that AES-FEM slightly outperformed GFDM in all the cases.

It should be noted that the linear systems for quadratic AES-FEM and linear FEM have nearly identical sparsity patterns. Additionally, the linear systems of quartic AES-FEM has only slightly more nonzeros than that of quadratic FEM, but it is significantly more accurate. Thus, when comparing matrices with similar numbers of DOFs and similar numbers of nonzeros, AES-FEM is often more accurate than FEM. As a result, AES-FEM sometimes requires less computational time than FEM [12,13, Chapter 6].

7. Conclusions and discussions

In this paper, we introduced the framework of *generalized weighted residual formulations* (*GWR*), which unifies generalized finite differences, Lagrange finite elements, and adaptive extended stencil FEM (AES-FEM). Under this framework, we presented a unified analysis of the *well-posedness* of these methods, which depend on the *quasiuniformity* and the consistency and stability of the trial functions and test functions. While the stability of the Lagrange basis functions in FEM depends on the well-shapedness of the elements, the GLP basis functions of GFDM and AES-FEM depend on the selections of the stencils, which can be adapted locally, due to the least-squares nature of the GLP basis functions. In addition, high-order AES-FEM requires only first-order meshes for its implementation, so its implementation is simpler than high-order finite elements. However, Lagrange FEM can achieve $\mathcal{O}(h^{p+1})$ convergence rate in L^2 norm. In contrast, GFDM and AES-FEM significantly simplify mesh generation, but it comes at the cost of a lower-order convergence rate, which is $\mathcal{O}(h^{p-1})$ with odd-degree GLP basis functions. However, with even-degree basis functions, GFDM can achieve $\mathcal{O}(h^p)$ convergence rate with nearly symmetric stencils, whereas AES-FEM can achieve $\mathcal{O}(h^p)$ convergence with nearly

symmetric local support. We presented numerical results to verify our theoretical analysis, and we showed that AES-FEM in general outperforms GFDM in terms of accuracy. For Neumann boundary conditions, we only considered polygonal domains. For curved geometries, we can overcome mesh quality dependency, namely the Ciarlet–Raviart condition, in AES-FEM by using techniques similar to GFDM, but a rigorous analysis of optimal convergence rates is challenging, which we plan to report elsewhere. One direction of future work is to investigate the development of new hybrid methods by mixing FEM and AES-FEM for different orders of terms.

Acknowledgments

This work was supported in part by DoD-ARO, USA under contract #W911NF0910306 and also in part under the Scientific Discovery through Advanced Computing (SciDAC) program in the US Department of Energy Office of Science, Office of Advanced Scientific Computing Research through subcontract #462974 with Los Alamos National Laboratory and under a subcontract with Argonne National Laboratory under Contract DE-AC02-06CH11357. The first author acknowledges the support of the Kenny Fund Fellowship of Saint Peter's University. Results were obtained using the high-performance LI-RED computing system at the Institute for Advanced Computational Science at Stony Brook University, USA, which was obtained through the Empire State Development grant NYS #28451.

Appendix A. Computation of GLP basis functions

Given a node $\boldsymbol{x}_0$, without loss of generality, assume it is at the origin of a local coordinate system. Let $\boldsymbol{\mathcal{P}}_k^{(p)}(\boldsymbol{x})$ denote the set of all d-dimensional monomials of degree p and lower; for example, $\boldsymbol{\mathcal{P}}_2^{(2)}(\boldsymbol{x}) = [1, x, y, x^2, xy, y^2]^T$. Let $\boldsymbol{D}_k^{(p)}$ be a diagonal matrix consisting of the fractional factorial part of the coefficients in the Taylor series corresponding to $\boldsymbol{\mathcal{P}}_k^{(p)}$; for example, $\boldsymbol{D}_2^{(2)} = \mathrm{diag}\,(1, 1, 1, 1/2, 1, 1/2)$. Let $\boldsymbol{c}$ be a vector containing the partial derivative of f evaluated at $\boldsymbol{x}_0$; for example, $\boldsymbol{c} = \left[f, f_x, f_y, f_{xx}, f_{xy}, f_{yy}\right]^T |_{\boldsymbol{x}=\boldsymbol{x}_0}$. Then, we may write the truncated Taylor series of a smooth function f as

$$f(\boldsymbol{x}) \approx \boldsymbol{c}^T \boldsymbol{D}_k^{(p)} \boldsymbol{\mathcal{P}}_k{}^{(p)}(\boldsymbol{x})\,. \tag{A.1}$$

Suppose there are n coefficients in $\boldsymbol{c}$, and the stencil about the point $\boldsymbol{x}_0$ contains m points, including the point $\boldsymbol{x}_0$. To obtain the jth basis function ϕ_j, let $f(\boldsymbol{x}_i) = \delta_{ij}$, the Kronecker delta function. Therefore, we obtain an $m \times n$ least squares problem

$$\boldsymbol{V}\boldsymbol{c}_j \approx \boldsymbol{e}_j, \tag{A.2}$$

where $\boldsymbol{e}_j$ denotes the jth column of the $m \times m$ identity matrix, and $\boldsymbol{V}$ is the generalized Vandermonde matrix. Eq. (A.2) may potentially be ill-conditioned and even rank deficient, even if $m \geq n$. We solve (A.2) by minimizing a weighted norm (or semi-norm)

$$\min_{\boldsymbol{c}} \left\|\boldsymbol{V}\boldsymbol{c}_j - \boldsymbol{e}_j\right\|_{\boldsymbol{W}} \equiv \min_{\boldsymbol{c}} \left\|\boldsymbol{W}\left(\boldsymbol{V}\boldsymbol{c}_j - \boldsymbol{e}_j\right)\right\|_2, \tag{A.3}$$

where $\boldsymbol{W}$ is an $m \times m$ diagonal weighting matrix, and it is a constant for a given node. In general, heavier weights are assigned to nodes that are closer to $\boldsymbol{x}_0$; for example,

$$w_i = \left(\frac{\|\boldsymbol{v}_i\|}{h} + \epsilon\right)^{-p/2}, \tag{A.4}$$

where ϵ is a small number, such as $\epsilon = 0.01$, for avoiding division by zero.

The matrix $\boldsymbol{WV}$ can be poorly scaled. We address this by right-multiplying a diagonal matrix $\boldsymbol{S}$. Let $\boldsymbol{a}_j$ denote the jth column of an arbitrary matrix $\boldsymbol{WV}$. A typical choice for the ith entry of $\boldsymbol{S}$ is either $1/\|\boldsymbol{a}_i\|_2$ or $1/\|\boldsymbol{a}_i\|_\infty$. This is known as *column equilibration* [50]. Note that a row equilibration or a general matrix equilibration should not be used, since it would undermine the weighting scheme $\boldsymbol{W}$. After weighting and scaling, the least-squares problem becomes

$$\min_{\boldsymbol{d}} \left\|\tilde{\boldsymbol{V}}\boldsymbol{d} - \boldsymbol{W}\boldsymbol{e}_j\right\|_2, \quad \text{where } \tilde{\boldsymbol{V}} \equiv \boldsymbol{WVS} \text{ and } \boldsymbol{d} \equiv \boldsymbol{S}^{-1}\boldsymbol{c}_j. \tag{A.5}$$

We solve the problem using the truncated QR factorization with column pivoting, where the pivoting scheme is customized to preserve low-degree terms. The solution of the least squares problem is $\boldsymbol{c}_j = \boldsymbol{S}\tilde{\boldsymbol{V}}^+\boldsymbol{W}\boldsymbol{e}_j$. The complete set of basis functions is then given by

$$\boldsymbol{\Phi} = \left(\boldsymbol{S}\tilde{\boldsymbol{V}}^+\boldsymbol{W}\right)^T \boldsymbol{D}\boldsymbol{\mathcal{P}}. \tag{A.6}$$

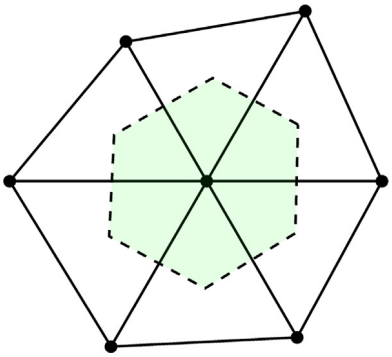

Fig. B.6. Example of 1-ring neighbor elements with the control volume of the center node in light green. (For interpretation of the references to color in this figure legend, the reader is referred to the web version of this article.)

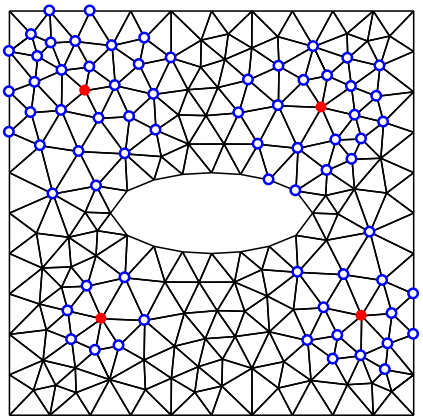

Fig. B.7. Examples of 2D stencils (blue circles) of four nodes (red dots) with neighborhood sizes of 1-ring, 1½-ring, 2-ring, and 2½-ring, counterclockwise from lower left.

Appendix B. Selection of stencils

To achieve high-order accuracy, a critical question is the selection of the stencils at each node for the construction of the GLP basis functions. We utilize meshes for speedy construction of the stencils. Given a simplicial mesh (i.e., a triangle mesh in 2D or a tetrahedral mesh in 3D), the *1-ring neighbor elements* of a node are defined to be the elements incident on the node. See Fig. B.6 for an example of the 1-ring neighborhood elements and the control volume of a node. The *1-ring neighborhood* of a node contains the nodes of its 1-ring neighbor elements [36]. For any integer $k \geq 1$, we define the $(k+1)$-*ring neighborhood* as the nodes in the k-ring neighborhood plus their 1-ring neighborhoods.

The 1-ring neighborhood of a node may supply a sufficient number of nodes for constructing quadratic GLP basis functions. However, 2- and 3-rings are often too large for cubic and quartic constructions. We refine the granularity of the stencils by using fractional rings. In 2D we use half-rings, as defined in [36]. For an integer $k \geq 1$, the $(k+1/2)$-*ring neighborhood* is the k-ring neighborhood together with the nodes of all the faces that share an edge with the k-ring neighborhood. See Fig. B.7 for an illustration. For 3D, we use 1/3- and 2/3-rings, as defined in [12]. For any integer $k \geq 1$, the $(k+1/3)$-*ring neighborhood* contains the k-ring neighborhood together with the nodes of all elements that share a face with the k-ring neighborhood. The $(k+2/3)$-*ring neighborhood* contains the k-ring neighborhood together with the nodes of all faces that share an edge with the k-ring neighborhood. See Fig. B.8 for an illustration of rings, one-third rings and two-third rings in 3D.

In practice, for degree-p basis functions in d-dimensional space, we typically choose the ring size $(p+1)/d$. This offers a good balance of accuracy, stability, and efficiency for basis functions up to degree 7. To illustrate, Table B.1 compares the average number of nodes in a given sized ring to the number of unknowns for a given degree in (A.2) on an example mesh. It can be seen that the $(p+1)/d$-ring size offers approximately 1.3 to 2 times the number of coefficients on average. If a particular neighborhood does not provide enough points, especially for nodes near boundaries, we further expand the stencil to a larger ring. The construction of the neighborhood requires an efficient mesh data structure, such as the Array-based Half-Facet (AHF) data structure [51].

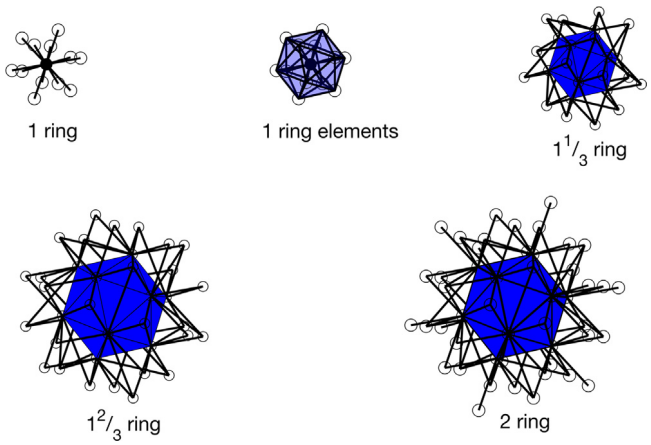

Fig. B.8. Examples of 3D stencils with 1-ring neighborhood, 1-ring elements, $1^1/_3$-ring neighborhood, $1^2/_3$-ring neighborhood and 2-ring neighborhood of the center node (in solid black).

Table B.1
Comparison of the average number of nodes per ring versus the number of coefficients for 2D (left) and 3D (right) Taylor polynomials.

Degree	#Coeffs.	Ring	#Nodes
2	6	$1^1/_2$	11.76
3	10	2	18.30
4	15	$2^1/_2$	29.23
5	21	3	37.47
6	28	$3^1/_2$	53.17
7	36	4	63.56

Degree	#Coeffs.	Ring	#Nodes
2	10	1	13.53
3	20	$1^1/_3$	29.44
4	35	$1^2/_3$	46.25
5	56	2	67.86
6	84	$2^1/_3$	121.54
7	120	$2^2/_3$	156.86

Appendix C. Overview of AES-FEM

Starting with a PDE with Dirichlet boundary conditions

$$\begin{aligned} \mathcal{L}u &= f \quad \text{on } \Omega \\ u &= u_D \quad \text{on } \Gamma_D \end{aligned} \tag{C.1}$$

AES-FEM can be derived from (3.8) as follows. AES-FEM uses generalized Lagrange polynomials as the basis functions $\{\phi_j\}$ and the traditional FEM hat functions as the test functions $\{\psi_i\}$. The solution u is approximated as $u = \sum u_j\phi_j$. As a concrete example, consider the Poisson equation. For a given node and corresponding test function ψ_i, we have

$$-\sum_{j=1}^{n} u_j \int_\Omega \nabla\psi_i \cdot \nabla\phi_j \, dV = \int_\Omega \psi_i f \, dV. \tag{C.2}$$

The stiffness matrix is assembled row by row. For each interior node, a stencil is selected (see Appendix B) and the GLP basis functions are calculated on that stencil (see Appendix A). If the stencil contains too few nodes, the stencil is enlarged (hence the word *adaptive* in the name adaptive extended stencil-FEM). The adaptive expansion of the stencil ensures the stability of the basis functions. The entries in the ith row of the stiffness matrix and the ith entry of the load vector are calculated using (C.2). Dirichlet boundary conditions are enforced strongly.

The degree of the basis functions controls the order of convergence of the method. Note that regardless of the degree of the GLP basis functions, AES-FEM can always use piecewise linear hat functions for the test functions, so it requires only first-order meshes, at least for Dirichlet boundary conditions.

Appendix D. Functional analysis and variational crimes

Unlike FDM, of which the convergence follows from the fundamental theorem of numerical analysis, proving convergence of FEM is more complicated. It requires an intricate integration of functional analysis and approximation theory, which were traditionally incompatible, and hence the term "variational crimes" coined by Strang [52,3].

D.1. Functional analysis of coercive PDEs

The convergence analysis of FEM is best known for coercive PDEs. One of the most fundamental results is the *Lax–Milgram lemma* [53,41, p. 83], which states that an FEM is *well-posed* (or *invertible*) for *bounded* and *coercive* bilinear forms. Its proof boils down to the *Riesz representation theorem* [41, p. 479] for C^0 functions and the *Poincaré inequality* [41, p. 489]. In practice, the boundedness and coercivity are satisfied on *quasiuniform* and *well-shaped* meshes. In terms of convergence, for simpler cases, such as FEM with Dirichlet boundary conditions, the error is bounded in L^2 norm, for which the most successful technique is the *Aubin–Nitsche duality argument* [54,55], a.k.a. "*Nitsche's trick*" [3, p. 166]. When approximation errors are involved, the convergence rates are often proven only in H^1 norm (see e.g. [9, p. 288] and [27, p. 199]).

D.2. Functional analysis of noncoercive PDEs

The generalization of functional analysis of FEM to noncoercive PDEs requires the use of Banach or Sobolev spaces. The best known result is the *Banach-Nečas-Babuška* (*BNB*) *theorem* [41, p. 84–85], attributed to Nečas [56] and Babuška [57], regarding the *invertibility* (or *well-posedness*). It generalizes the *Lax–Milgram lemma*. The theorem states that an FEM with a specific trial space Φ and test space Ψ is *invertible* if and only if

$$\exists \alpha > 0, \qquad \inf_{\phi \in \Phi \setminus \{0\}} \sup_{\psi \in \Psi \setminus \{0\}} \frac{a(\phi, \psi)}{\|\phi\|_{\Phi} \|\psi\|_{\Psi}} \geq \alpha \tag{D.1}$$

and

$$\forall \psi \in \Phi, \qquad \sup_{\phi \in \Phi \setminus \{0\}} |a(\phi, \psi)| = 0 \Longrightarrow \psi = 0, \tag{D.2}$$

where $\|\cdot\|_{\Phi}$ and $\|\cdot\|_{\Psi}$ are some norms associated with the spaces Φ and Ψ over Ω, respectively. An assumption of the BNB theorem is the *boundedness* of the bilinear form [41, p. 82]

$$\exists C < \infty, \qquad \sup_{\phi \in \Phi \setminus \{0\}} \sup_{\psi \in \Psi \setminus \{0\}} \frac{a(\phi, \psi)}{\|\phi\|_{\Phi} \|\psi\|_{\Psi}} \leq C \tag{D.3}$$

under some continuity requirements on Φ and Ψ (such as C^0 continuity). Eq. (D.1) is known as the *inf–sup condition*. For coercive problems, $\|\cdot\|_{\Phi}$ and $\|\cdot\|_{\Psi}$ in (D.1) typically correspond to some norm over Ω. In practice, the boundedness and inf–sup conditions also require *quasiuniform* and *well-shaped* meshes. Since the invertibility condition is purely algebraic, the solutions may suffer from spurious oscillations for noncoercive PDEs.

D.3. Variational crimes

In the classical functional analysis, a deviation from exact computations or conforming FEM is considered a "variational crime" [9,3]. This includes interpolation errors that are not intrinsic in the L^p (or H^1) norms, numerical integration errors, rounding errors, etc. A fundamental "crime" is the loss of continuity, which is introduced by *nonconforming finite elements* [9, Section 10.3]. AES-FEM involves a similar but more severe "crime" due to its use of least-squares-based local trial functions, making the classical duality argument inapplicable.

References

[1] R.J. LeVeque, Finite Difference Methods for Ordinary and Partial Differential Equations: Steady-State and Time-Dependent Problems, Vol. 98, SIAM, 2007.
[2] J.C. Strikwerda, Finite Difference Schemes and Partial Differential Equations, SIAM, 2004.
[3] G. Strang, G.J. Fix, An Analysis of the Finite Element Method, Vol. 212, Prentice-Hall Englewood Cliffs, NJ, 1973.
[4] O.C. Zienkiewicz, R.L. Taylor, J.Z. Zhu, The Finite Element Method: Its Basis and Fundamentals, seventh ed., Butterworth-Heinemann, 2013.
[5] B. Cockburn, G.E. Karniadakis, C.-W. Shu, The Development of Discontinuous Galerkin Methods, Springer, Berlin Heidelberg, 2000.
[6] B. Rivière, Discontinuous Galerkin Methods for Solving Elliptic and Parabolic Equations: Theory and Implementation, SIAM, 2008.
[7] R.J. LeVeque, Finite Volume Methods for Hyperbolic Problems, Vol. 31, Cambridge University Press, 2002.
[8] R. Li, Z. Chen, W. Wu, Generalized Difference Methods for Differential Equations: Numerical Analysis of Finite Volume Methods, CRC Press, 2000.
[9] S.C. Brenner, R. Scott, The Mathematical Theory of Finite Element Methods, Vol. 15, Springer, 2008.
[10] C.-W. Shu, High-order finite difference and finite volume WENO schemes and discontinuous Galerkin methods for CFD, Int. J. Comput. Fluid Dyn. 17 (2) (2003) 107–118, http://dx.doi.org/10.1080/1061856031000104851.

[11] B. Costa, W.S. Don, High order hybrid central-WENO finite difference scheme for conservation laws, J. Comput. Appl. Math. 204 (2) (2007) 209–218, http://dx.doi.org/10.1016/j.cam.2006.01.039.
[12] R. Conley, T.J. Delaney, X. Jiao, Overcoming element quality dependence of finite elements with adaptive extended stencil FEM (AES-FEM), Internat. J. Numer. Methods Engrg. (2016) http://dx.doi.org/10.1002/nme.5246.
[13] R. Conley, Overcoming Element Quality Dependence of Finite Element Methods (Ph.D. thesis), Department of Applied Mathematics and Statistics, Stony Brook University, Stony Brook, NY, 2016.
[14] J. Benito, F. Ureña, L. Gavete, Solving parabolic and hyperbolic equations by the generalized finite difference method, J. Comput. Appl. Math. 209 (2) (2007) 208–233, http://dx.doi.org/10.1016/j.cam.2006.10.090.
[15] V. Thomée, From finite differences to finite elements a short history of numerical analysis of partial differential equations, in: Numerical Analysis: Historical Developments in the 20th Century, Elsevier, 2001, pp. 361–414, http://dx.doi.org/10.1016/S0377-0427(00)00507-0.
[16] T.F. Chan, D.E. Foulser, Effectively well-conditioned linear systems, SIAM J. Sci. Stat. Comput. 9 (6) (1988) 963–969, http://dx.doi.org/10.1137/0909067.
[17] S. Christiansen, P.C. Hansen, The effective condition number applied to error analysis of certain boundary collocation methods, J. Comput. Appl. Math. 54 (1) (1994) 15–36, http://dx.doi.org/10.1016/0377-0427(94)90391-3.
[18] Z.-C. Li, C.-S. Chien, H.-T. Huang, Effective condition number for finite difference method, J. Comput. Appl. Math. 198 (1) (2007) 208–235, http://dx.doi.org/10.1016/j.cam.2005.11.037.
[19] M.R. Visbal, D.V. Gaitonde, On the use of higher-order finite-difference schemes on curvilinear and deforming meshes, J. Comput. Phys. 181 (1) (2002) 155–185, http://dx.doi.org/10.1006/jcph.2002.7117.
[20] L. Cueto-Felgueroso, I. Colominas, X. Nogueira, F. Navarrina, M. Casteleiro, Finite volume solvers and moving least-squares approximations for the compressible Navier–Stokes equations on unstructured grids, Comput. Methods Appl. Mech. Engrg. 196 (45–48) (2007) 4712–4736, http://dx.doi.org/10.1016/j.cma.2007.06.003.
[21] H. Liu, X. Jiao, WLS-ENO: Weighted-least-squares based essentially non-oscillatory schemes for finite volume methods on unstructured meshes, J. Comput. Phys. 314 (2016) 749–773, http://dx.doi.org/10.1016/j.jcp.2016.03.039.
[22] R.H. Macneal, An asymmetrical finite difference network, Q. Appl. Math. 11 (3) (1953) 295–310.
[23] F.U. Prieto, J.J.B. Muñoz, L.G. Corvinos, Application of the generalized finite difference method to solve the advection–diffusion equation, J. Comput. Appl. Math. 235 (7) (2011) 1849–1855, http://dx.doi.org/10.1016/j.cam.2010.05.026.
[24] L. Gavete, F. Ureña, J.J. Benito, A. García, M. Ureña, E. Salete, Solving second order non-linear elliptic partial differential equations using generalized finite difference method, J. Comput. Appl. Math. 318 (2017) 378–387, http://dx.doi.org/10.1016/j.cam.2016.07.025.
[25] F. Ureña, L. Gavete, A. García, J. Benito, A. Vargas, Solving second order non-linear parabolic PDEs using generalized finite difference method (GFDM), J. Comput. Appl. Math. 354 (2019) 221–241, http://dx.doi.org/10.1016/j.cam.2018.02.016.
[26] B.A. Finlayson, The Method of Weighted Residuals and Variational Principles, Academic Press, New York, 1973.
[27] P. Ciarlet, The Finite Element Method for Elliptic Problems, SIAM, 2002.
[28] G. Fix, G. Strang, Fourier analysis of the finite element method in Ritz-Galerkin theory, Stud. Appl. Math. 48 (3) (1969) 265–273, http://dx.doi.org/10.1002/sapm1969483265.
[29] J. Douglas Jr., T. Dupont, M.F. Wheeler, An L^∞ estimate and a superconvergence result for a Galerkin method for elliptic equations based on tensor products of piecewise polynomials, RAIRO Anal. Numer. 8 (1974) 61–66, http://dx.doi.org/10.1051/m2an/197408R200611.
[30] J. Douglas Jr., T. Dupont, Superconvergence for Galerkin methods for the two point boundary problem via local projections, Numer. Math. 21 (3) (1973) 270–278, http://dx.doi.org/10.1007/BF01436631.
[31] P.S. Jensen, Finite difference techniques for variable grids, Comput. Struct. 2 (1–2) (1972) 17–29, http://dx.doi.org/10.1016/0045-7949(72)90020-X.
[32] N. Perrone, R. Kao, A general finite difference method for arbitrary meshes, Comput. Struct. 5 (1) (1975) 45–57, http://dx.doi.org/10.1016/0045-7949(75)90018-8.
[33] T. Liszka, J. Orkisz, The finite difference method at arbitrary irregular grids and its application in applied mechanics, Comput. Struct. 11 (1–2) (1980) 83–95, http://dx.doi.org/10.1016/0045-7949(80)90149-2.
[34] G.M. Phillips, Interpolation and Approximation By Polynomials, Vol. 14, Springer, 2003.
[35] P.G. Ciarlet, P.-A. Raviart, Interpolation theory over curved elements, with applications to finite element methods, Comput. Methods Appl. Mech. Engrg. 1 (2) (1972) 217–249, http://dx.doi.org/10.1016/0045-7825(72)90006-0.
[36] X. Jiao, H. Zha, Consistent computation of first-and second-order differential quantities for surface meshes, in: ACM Symposium on Solid and Physical Modeling, ACM, 2008, pp. 159–170, http://dx.doi.org/10.1145/1364901.1364924.
[37] Y. Li, Q. Chen, X. Wang, X. Jiao, WLS-ENO remap: Superconvergent and non-oscillatory weighted least squares data transfer on surfaces, J. Comput. Phys. (2019) submitted for publication. Preprint available on https://arxiv.org/abs/1912.00268.
[38] J. Humpherys, T.J. Jarvis, E.J. Evans, Foundations of Applied Mathematics, Volume I: Mathematical Analysis, SIAM, 2017.
[39] R. Sevilla, S. Fernández-Méndez, A. Huerta, NURBS-enhanced finite element method (NEFEM), Internat. J. Numer. Methods Engrg. 76 (1) (2008) 56–83, http://dx.doi.org/10.1002/nme.2311.
[40] L. Gavete, M.L. Gavete, F. Ureña, J.J. Benito, An approach to refinement of irregular clouds of points using generalized finite differences, Math. Probl. Eng. 2015 (2015) http://dx.doi.org/10.1155/2015/283757.
[41] A. Ern, J.-L. Guermond, Theory and Practice of Finite Elements, Vol. 159, Springer Science & Business Media, 2013.
[42] X. Jiao, D. Wang, Reconstructing high-order surfaces for meshing, Eng. Comput. 28 (4) (2012) 361–373, http://dx.doi.org/10.1007/s00366-011-0244-8.
[43] I. Singer, Linear functionals on the space of continuous mappings of a compact Hausdorff space into a Banach space, Rev. Math. Pures Appl. 2 (1957) 301–315.
[44] I. Babuška, A. Aziz, On the angle condition in the finite element method, SIAM J. Numer. Anal. 13 (2) (1976) 214–226, http://dx.doi.org/10.1137/0713021.
[45] J.R. Shewchuk, What is a good linear finite element? - Interpolation, conditioning, anisotropy, and quality measures, Tech. Rep. in: Proc. of the 11th International Meshing Roundtable, 2002.
[46] J.R. Shewchuk, Delaunay refinement algorithms for triangular mesh generation, Comput. Geom. 22 (1–3) (2002) http://dx.doi.org/10.1016/S0925-7721(01)00047-5.
[47] T.-W. Ma, Higher chain formula proved by combinatorics, Electron. J. Combin. 16 (1) (2009) N21, http://dx.doi.org/10.37236/259.
[48] L. Wahlbin, Superconvergence in Galerkin Finite Element Methods, Springer, 1995.
[49] MathWorks, MATLAB Partial Differential Equations Toolbox R2018a, 2018, https://www.mathworks.com/products/pde.html.
[50] A. van der Sluis, Condition numbers and equilibration of matrices, Numer. Math. 14 (1) (1969) 14–23, http://dx.doi.org/10.1007/BF02165096.
[51] V. Dyedov, N. Ray, D. Einstein, X. Jiao, T.J. Tautges, AHF: Array-based half-facet data structure for mixed-dimensional and non-manifold meshes, in: Proceedings of the 22nd International Meshing Roundtable, Springer, Orlando, Florida, 2014, pp. 445–464, http://dx.doi.org/10.1007/978-3-319-02335-9_25.

[52] G. Strang, Variational crimes in the finite element method, in: The Mathematical Foundations of the Finite Element Method with Applications to Partial Differential Equations, Academic Press, New York, 1972, pp. 689–710.
[53] P.D. Lax, A.N. Milgram, Parabolic equations: Contributions to the theory of partial differential equations, Ann. Math. Stud. (1954).
[54] J.P. Aubin, Behavior of the error of the approximate solutions of boundary value problems for linear elliptic operators by Galerkin's and finite difference methods, Ann. Sc. Norm. Super Pisa Cl. Sci. 21 (4) (1967) 599–637.
[55] J. Nitsche, Ein kriterium für die quasi-optimalität des ritzschen verfahrens, Numer. Mate. 11 (4) (1968) 346–348.
[56] J. Nečas, Sur une méthode pour résoudre les équations aux dérivées partielles du type elliptique, voisine de la variationnelle, Ann. Sc. Norm-Sci. 16 (4) (1962) 305–326.
[57] I. Babuska, A.K. Aziz, Survey lectures on the mathematical foundations of the finite element method, in: The Mathematical Foundations of the Finite Element Method with Applications to Partial Differential Equations, Academic, 1972, pp. 3–359.